ABSTRACT

Title of Document: ADVECTION-DIFFUSION CONTROLLED LITHIUM ISOTOPIC DISTRIBUTION IN CONTACT AUREOLES: —A CASE STUDY FROM THE FLORENCE COUNTY PEGMATITES, WISCONSIN

Xiao-Ming Liu, M.S., 2009

Directed By: Professor Roberta L. Rudnick and Assistant Professor Saswata Hier-Majumder Department of Geology

Stable isotopes are useful tracers of fluid-rock interactions in contact aureole settings. To date, only a few case studies have used Li isotopes to study fluid-rock interactions in contact aureole settings. These studies highlight the very large Li isotopic fractionation that can be generated in these settings via diffusion of Li from the pluton into the country rocks, but none of these studies have generated a complete and detailed section of the contact aureole needed to understand the Li distributions. Here, I report the results from a combination of Li isotope analyses and 2-D advection-diffusion modeling for two detailed profiles through country rocks adjacent to Li-rich pegmatite dikes in the Florence County pegmatite field. The results show that the Li concentration and isotopic distribution in the two contact profiles is consistent with fluid infiltration and diffusion of Li through a grain boundary fluid from the pegmatites into their country rocks.

ADVECTION-DIFFUSION CONTROLLED LITHIUM ISOTOPIC DISTRIBUTION IN CONTACT AUREOLES:
—A CASE STUDY FROM THE FLORENCE COUNTY PEGMATITE, WISCONSIN

By

Xiao-Ming Liu

Thesis submitted to the Faculty of the Graduate School of the
University of Maryland, College Park, in partial fulfillment
of the requirements for the degree of
Master of Science
2009

Advisory Committee:
Assistant Professor Saswata Hier-Majumder, Chair
Professor Roberta L. Rudnick, Co-Chair
Assistant Professor Sarah Penniston-Dorland

Acknowledgements

I would like to thank my advisors, Roberta Rudnick and Sash Hier-Majumder, without whom I would not be able to reach this point and enjoy my thesis research. Roberta introduced me to the lithium isotopes analysis, from weighing samples to operating the mass spectrometer. At the same time, she taught me to keep big pictures in my mind while doing my research. Sash introduced me to the numerical modeling, from helping me check out my codes to discussing the physical processes in the model. Also, Sash has been a wonderful source of encouragement, offering good academic and life advice.

I thank my committee member, Sarah Penniston-Dorland, for offering great insights on this project.

Mona-Liza Sirbescu is greatly appreciated for helping with the field work and additional sampling. Her enthusiasm is impressive and great help for this project.

I would also like to thank Bill McDonough for helping with ICP-MS analysis, Richard Ash for helping with both whole rock and laser ablation analysis, and Phil Piccoli for helping with electron microprobe work. I also appreciate Lin Qiu's help with Li analysis; Igor Puchtel's help in the clean lab and Jingao Liu's help for sample preparations. I thank Madalyn Blondes for commenting on an earlier version of this thesis.

I would also like to thank all friends from the Department of Geology, UMD for offering a supportive environment so that I enjoyed my research.

Finally, I want to thank my parents for their love and encouragement.

Table of Contents

List of Tables

List of Figures

Chapter 1: Introduction

Fluid flow plays an important role in the continental crust, at least to depths of 10 ~ 15 km, because during fluid-rock interactions, fluids may change various physical and chemical properties of the crust, such as the thermal structure and chemical composition (e.g., Ague, 2003; Deming, 1994; Ferry, 1994). Fluid-rock interactions in contact aureoles have been studied intensively. Stable isotopes are especially useful for tracing flow fluid through metamorphic country rocks (Baumgartner and Valley, 2001 and references therein).

Oxygen isotopes have been widely used in studying metamorphic fluid flow in contact aureole settings. Models of one-dimensional oxygen isotope transport in homogeneous porous rocks provide basic understanding of fluid-rock interactions (e.g., Bickle and McKenzie, 1987; Bowman and Willett, 1991). However, because flow fluid direction (up-down and towards-away from pluton) (Ferry, 1994; Ferry et al., 2002) and permeability structure of the country rocks play important roles in controlling oxygen isotope distribution (Cui et al., 2001), 1-D fluid flow models are often not adequate for describing the isotope transport processes. 2-D flow fluid models can incorporate fluid infiltration direction and structure of country rocks (e.g., permeability structure) during contact metamorphism. Starting from the pioneering work of Norton and Taylor (1979), 2-D reactive flow models for oxygen isotopes have successfully reproduced heterogeneous fluid flow patterns (e.g., Cook et al., 1997; Cui et al., 2002).

Lithium has a few advantages as a tracer in studying fluid flow in contact aureoles. First, Li is fluid mobile and moves faster (e.g., has a higher diffusion

coefficient) than most geochemical tracers (Richter et al., 2003). Thus, Li can trace diffusive processes on a shorter timescale and/or greater length scale compared to other isotopic tracers. Second, lithium is moderately incompatible, so it prefers melts to rocks during partial melting and becomes enriched in evolved plutons, such as Li-rich granitic pegmatites, which can act as a Li source for tracing fluid flow in the contact aureole. Third, there is a large mass difference (~17%) between the two stable isotopes of Li, which gives rise to significant isotopic fractionation in various geological environments, especially during diffusion. Lastly, the analysis of Li isotopes has improved to the point where precision is routinely $\leq 1‰$, allowing clear distinction of natural isotopic fractionation from analytical uncertainty (Tomascak, 2004). Therefore, lithium can be used as a geochemical tracer for fluid-rock interactions in the continental crust.

Recent observations in some contact aureoles around igneous intrusions, such as that of the Tin Mountain pegmatite, South Dakota (Teng et al., 2006a), and the Ilimaussaq Intrusion, Greenland (Marks et al., 2007), reveal large and systematic changes in δ^7Li values, which is defined as:

$$\delta^7Li = [(^7Li/^6Li)_{sample}/(^7Li/^6Li)_{standard}-1] \times 1000.$$

In the Tin Mountain case, both Li concentration and δ^7Li decrease dramatically with distance from the contact. A 1-D diffusion model matches the geochemical observations, indicating diffusion-driven lithium isotopic fractionation through pore fluids (Teng et al., 2006a). However, the profile ends at ~ 10 m distance from the contact, and so the total distance over which Li has moved is unknown. By contrast, at the Onawa pluton in Maine, no obvious lithium isotopic fractionation was observed in the surrounding contact metamorphic aureole (Teng et al., 2007). This may be due to the fact that the granodiorite pluton has lower Li concentration relative

to its pelitic country rock, driving Li diffusion towards the pluton, and/or the much greater length scale of the measured section (~1.5 km) compared to the previous example. For the Ilimaussaq contact aureole, a 1-D diffusion model can explain Li isotopic distribution in the granitic country rock. However, it fails to explain δ^7Li distribution in the augite syenite intrusion. A two-stage model is required, where, in addition to the diffusion process, an external fluid source with higher δ^7Li shifts the augite syenite to higher δ^7Li values (Marks et al., 2007). This contrast in Li distribution between the three previously studied aureoles raises the question: what are the most important factors controlling Li isotope distribution in contact aureole settings?

The objectives of this study are to determine the most significant parameters that influence lithium isotopic distribution in contact aureoles and to further develop Li isotopes as a tracer in studying fluid flow processes in the crust. Towards this end, lithium concentration and isotopic composition of pegmatite intrusions and their country rocks were measured for the Florence County pegmatites, Wisconsin. Interpretation of the results was aided by a 2-D fluid flow numerical model, which allows identification of the most important parameters influencing Li distribution in these settings and provides constraints on those parameters.

Chapter 2: Geological Background and Samples

Samples in this study are from Florence County in northeastern Wisconsin, ~15km south of the border with northern Michigan (Figure 1). Here, pegmatite dikes intruded into rocks of the Penokean Orogen, a 1400 km long fold-and-thrust belt that formed during accretion and collision of the early Proterozoic Wisconsin Magmatic Terrane onto the southern margin of the Archean Superior Province. The pegmatite field is located about 5 km south of the Niagara Fault Zone (Sirbescu et al., 2008, and references therein).

The source of the Florence county pegmatite dikes is believed to be ~1760 Ma post-tectonic granites that were intruded at depths of 10-11 km (Holm et al., 2005). The country rocks of the pegmatites belong to the 1866 ± 39 Ma (Sims et al., 1992) Quinnesec Formation, which is an early Penokean unit composed of metavolcanic rocks. These rocks are regionally metamorphosed to greenschist and amphibolite facies. Minor metasedimentary layers, such as quartz-mica schists, iron formation, and quartzites, are present (Sirbescu et al., 2008).

Samples were collected adjacent to pegmatites, namely, the road cut that exposes the King-X pegmatite (hereafter referred to as the KX Road Cut profile) and Animikie Red Ace Profile (ARA profile). In addition, regional samples were collected far away from any known pegmatites (e.g., a few hundred meters to several thousand meters away from the pegmatites, Figure 2.). Thus, the regional samples are regarded as unaffected by pegmatite intrusions. Detailed petrographic descriptions of pegmatite, country rock and regional samples are provided in Table A1.

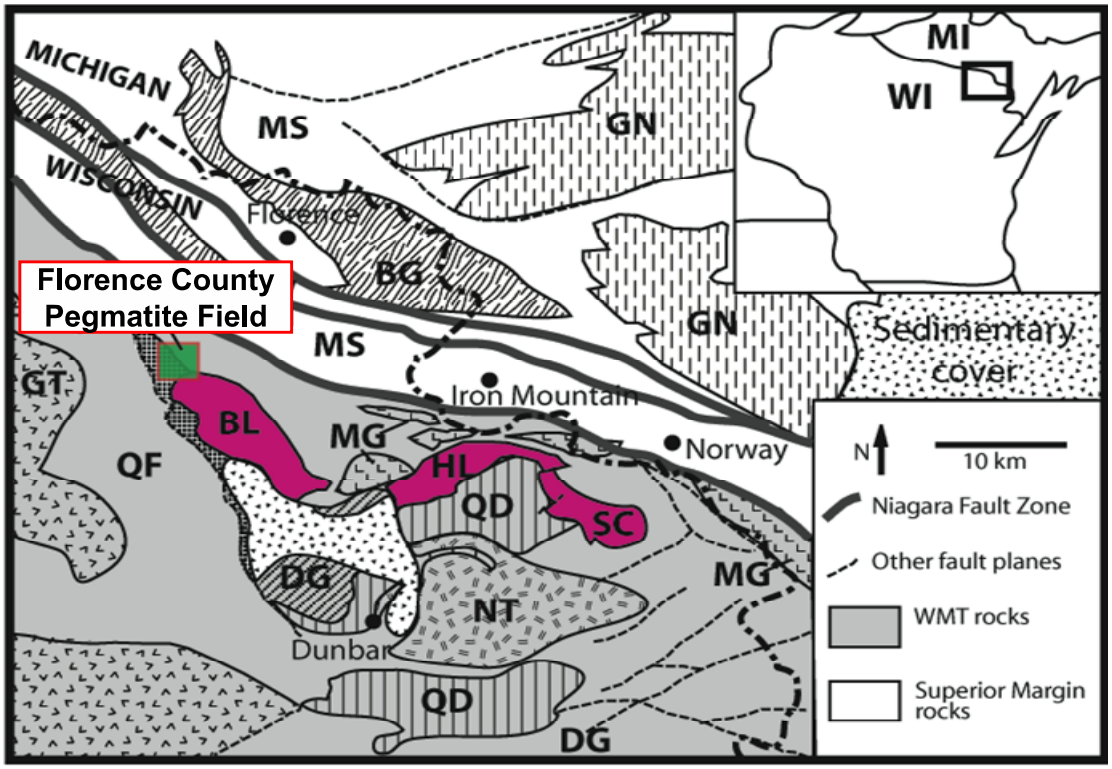

Figure 1. Geological map of northeastern Wisconsin including the Florence county pegmatite field (from Sirbescu et al., 2008). Superior Province Margin units: MS Michigamme Slate, BG Badwater Greenstone, GN Undifferentiated gneisses. Wisconsin Magmatic Terrane (WMT): Dunbar dome granitoids: BL Bush Lake Granite, HL Hoskin Lake Granite, SC Spike Creek Granite, QD Quartz diorite, DG Dunbar Gneiss; GT undifferentiated granite and tonalite; and metamorphic units: QF Quinnesec Formation metavolcanics, MR Metasedimentaryrocks, MG Metagabbro, and NT Newingham Tonalite.

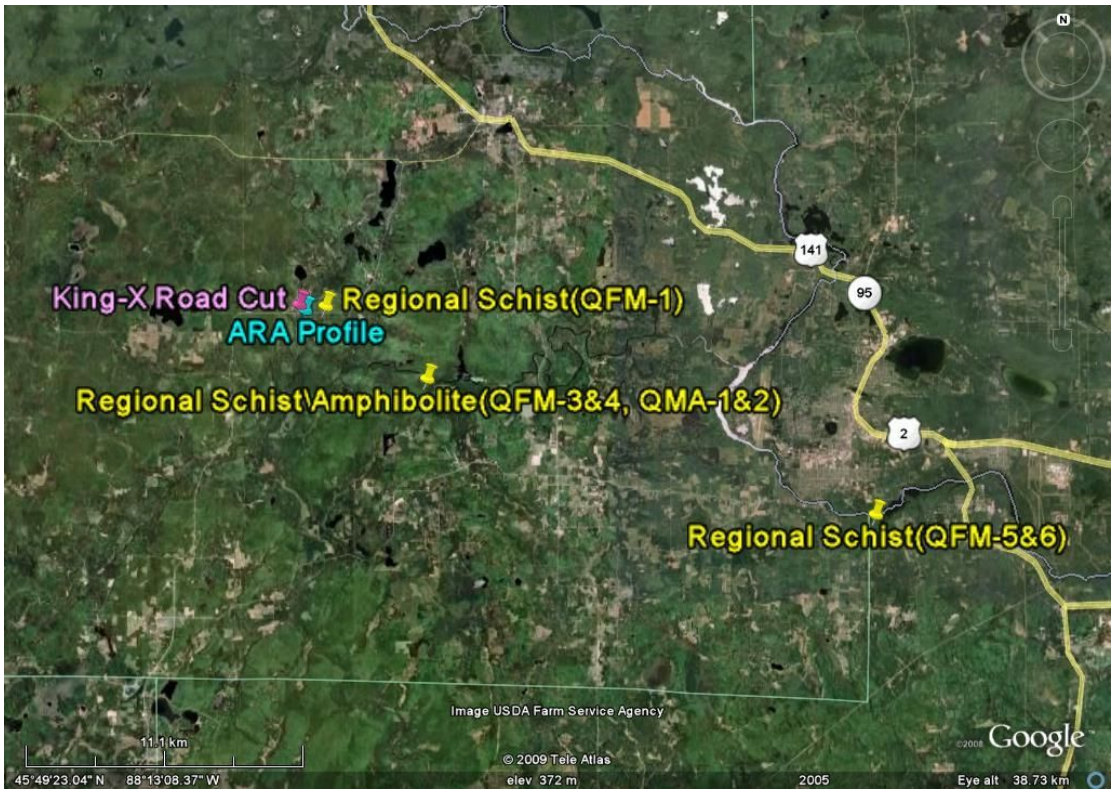

Figure 2. Google map image of sample locations.

2.1 King-X Road Cut Profile

The King-X road cut profile is made up of the pegmatite intrusion into variable types of country rocks (Figure 3, Figure 5A, and Figure 5B): schists occur closest to the pegmatite and these are followed by carbonate-bearing amphibolite that is interbedded with quartzite. On the whole, the KX profile shows banded lithological variations sub-parallel to the road cut.

The King-X pegmatite (KX) is ~3 m wide and occurs at the west end of the road cut (Figure 3). From field observation, the KX is composed of dark gray feldspar/quartz, black tourmaline and spodumene. The single thin-section sample from the KX pegmatite is mainly composed of feldspar and quartz, with muscovite as an accessory mineral.

The country rocks consist of various lithologies, including amphibolite, biotite schist, and quartzite. The amphibolite consists of alternating layers of dark amphibole and white carbonate; biotite schists consist of foliated biotite and feldspar/quartz/carbonate, and quartzites contain mainly quartz. In thin-section, amphibolites are mainly composed of amphibole, feldspar, quartz and carbonate; some amphibolites contain biotite, chlorite, opaques, and titanite. Chlorite mostly occurs on the rims of amphibole, indicating that chlorite is likely to be a secondary mineral produced via alteration. Biotite schists are composed of biotite, quartz, feldspar, and carbonate with or without chlorite, epidote, opaques, and titanite. Quartzites contain quartz, amphibole and opaques with or without biotite, carbonate, chlorite, and titanite. In all samples, chlorite, which is a common accessory mineral in the KX country rocks, appears to be an alteration product of amphibole (Figure 6).

A ~0.1 m wide quartz vein (named LP) nearly vertically intruded into the country rocks at ~16.5 m away from the KX pegmatite. The LP quartz vein does not

show any sign of deformation, and the relative timing of intrusion between the KX pegmatite and the LP quartz vein is unknown. Twenty-nine country rock samples were collected within a ~40 m wide traverse along the KX road cut (Figure 3).

Figure 3. Field photos of the KX profile. Upper panel shows the KX pegmatite with blue tape marking pegmatite-country rock boundaries; lower panel shows the right side of the KX profile.

2.2 Animikie Red Ace Profile

The Animikie Red Ace (ARA) profile is composed of two pegmatite dikes separated by ~ 60 m of country rocks (Figure 4, Figure 5C and D). The larger pegmatite, P1 is ~2.5 m wide and the smaller one, P2, is ~0.6 m wide. P1 is mineralogically zoned and likely cooled to < 400 ^{o}C rapidly (within 50 days) as discussed in the previous study of Sirbescu et al. (2008). The relative timing of intrusion of these two dikes is not known. Two bulk samples were collected from the P1 pegmatite and one sample was collected from the P2 pegmatite. One P1 sample, ARA1a, is massive, with feldspar, quartz and lepidolite, and minor tourmaline. The other P1 sample, ARA1b, is composed of tourmaline, quartz, feldspar and lepidolite. The P2 pegmatite sample, 08-P-06, consists of fine-grained feldspar, quartz, and micas with rare blue apatite and black tourmaline. In thin-section, ARA1a is mainly composed of feldspar and quartz and ARA1b is composed of tourmaline, quartz, feldspar with minor muscovite. The smaller pegmatite (P2), 08-P-06, consists of feldspar, quartz, and epidote.

The ARA country rocks display vertical foliation that is roughly perpendicular to the exposure surface. The country rock consists of schist within the first 45 m from the contact with P1 and amphibolite for the rest of the contact profile to P2. In hand samples, schists consist of fine-grained biotite and feldspar/quartz and amphibolites contain amphibole and feldspar/quartz with or without garnet. In thin-section, biotite schists are mainly composed of quartz, biotite, and feldspar with or without amphibole, carbonate, chlorite, epidote, muscovite and opaques. Amphibole and epidote are unusual minerals for a meta-pelite, suggesting these rocks may be meta-volcanic rocks. Amphibolites are mainly composed of amphibole, feldspar and quartz, with/without biotite, epidote and opaques. The presence of epidote, as well as

chlorite, may indicate alteration, especially in the case of chlorite, which is mostly present on the rims of the amphibole. Fifteen country rock samples were collected within a ~60 m wide traverse along the ARA profile.

Figure 4. Field photos of the ARA profile. Upper panel shows the ARA pegmatite (P1) with a white tape marking the pegmatite-country rock boundary (The pegmatite is on the lower-right side of the contact); lower panel shows a close look of the ARA country rock.

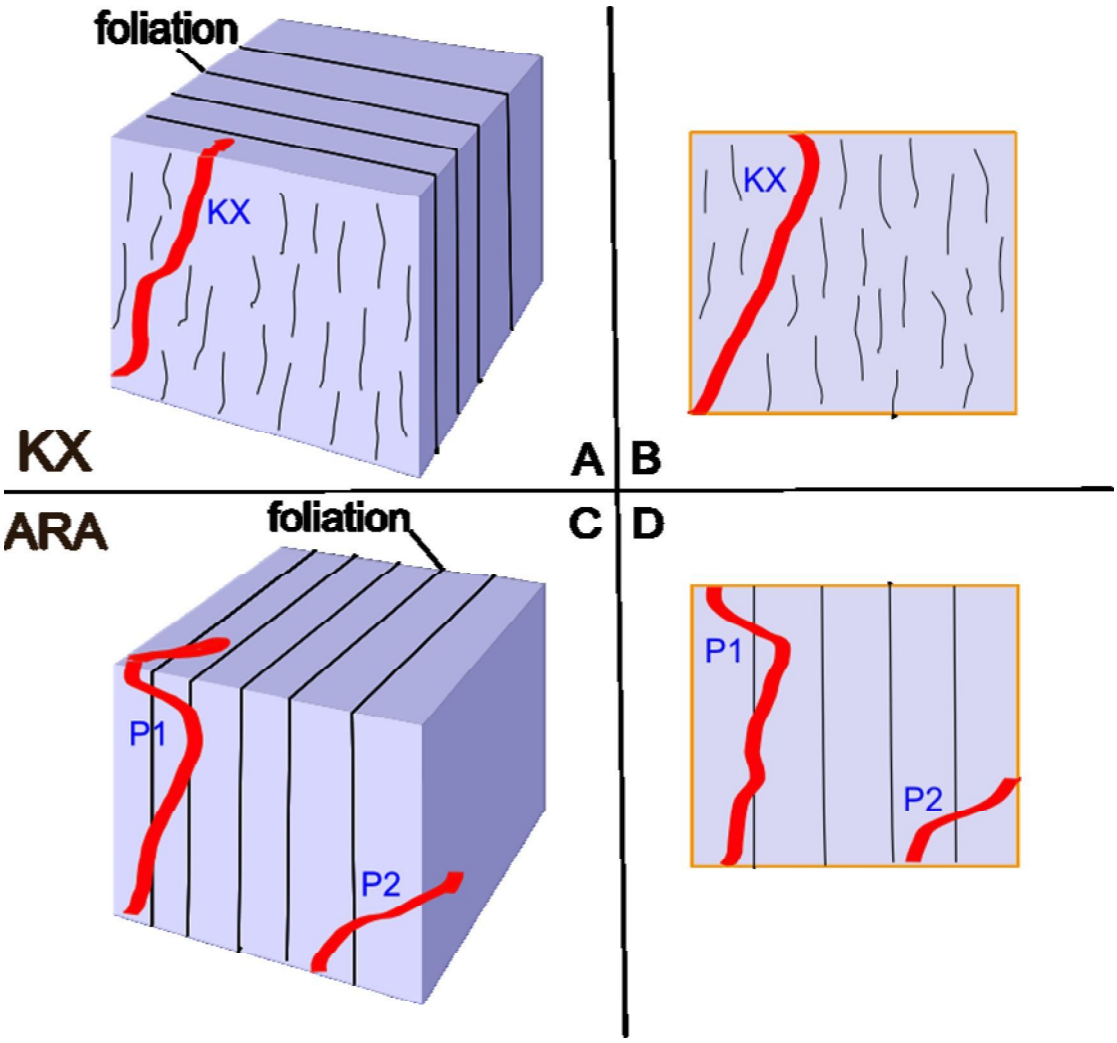

Figure 5. Schematic field geometry of the pegmatites and their country rocks. Red represents pegmatite dikes and blue areas are country rocks that the pegmatites intruded into. Solid and dashed black lines represent foliations and lithological layers, respectively. A and B are 3-D and 2-D model geometry of King-X road cut profile, respectively. C and D are 3-D and 2-D model geometry of Animikie Red Ace profile, respectively.

2.3 Regional Samples

Regional samples were collected from outcrops that are hundreds of meters to several kilometers away from the pegmatites. Five schists and two amphibolites were collected. In thin-section, both schists and amphibolites have similar mineral phases with their counterparts from the KX and ARA profiles, except that regional amphibolites lack carbonate. Schists are mainly composed of quartz, biotite, and feldspar, with or without amphibole, carbonate, chlorite, epidote, and opaques. Amphibolites are mainly composed of amphibole, feldspar and quartz, with or

without biotite, chlorite and opaques. Unlike the profile samples, the regional samples show no obvious evidence of alteration (Figure 6). Chlorite in regional samples is unlikely to be an alteration product, rather, it appears to be a primary mineral because chlorite mostly does not appear on the rim of the amphibole.

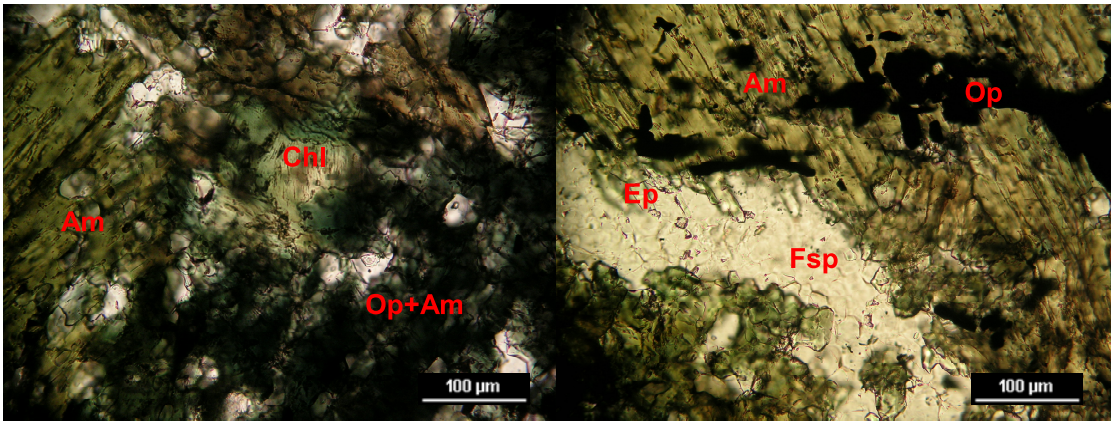

Figure 6. Petrographic comparison between one of the KX amphibolite samples (LP8, left panel) and one regional amphibolite (QMA1, right panel). Symbols: Am, Amphibole; Chl, Chlorite; Fsp, Feldspar; Op, Opaque.

Chapter 3: Analytical Methods

3.1 Lithium Analyses of Whole Rocks

There are three main steps for analysis of lithium concentration and isotopic composition in this study: Sample dissolution, column chemistry and instrumental analysis. Detailed procedures for sample dissolution and column chemistry are described in Rudnick et al. (2004). Detailed instrumental analysis can be found in Teng et al. (2004).

Rock samples were cut and then ground to powders using a corundum jaw crusher after the weathered surfaces of samples were first sawn off. Rock powders were dissolved using a roughly 3:1 mixture of HF and HNO_3 in Savillex® screw-top beakers on the hot plate ($T \approx 90^oC$), followed by HNO_3 and HCl addition until all powder was dissolved and the solution was clear.

Solutions were purified using cation exchange columns (BioRad AG50W-x12). Four chromatographic columns were used, modified from the procedure described in Moriguti and Nakamura (1998). The first two columns eliminate major element cations in sample solutions with 2.5M HCl and 0.15M HCl, respectively. The third column separates Na from Li with 30% ethanol in 0.5M HCl and the fourth column is the same as the third one.

Whole rock solutions were analyzed using the Nu Plasma Multi Collector-Inductively Coupled Plasma-Mass Spectrometer (MC-ICP-MS) at the University of Maryland. Standard bracketing, utilizing L-SVEC, was used for all the analyses. The Li isotopic composition is reported as δ^7Li. The external precision, based on 2σ of repeat runs of pure Li standard solutions, is $\leqslant \pm 1.0‰$. For example,

IRMM-016 run during the course of these analyses gives δ^7Li = -0.5 ± 0.9‰ (2 σ, n = 25); and the in-house standard UMD-1 gives δ^7Li = 54.4 ± 1.0‰ (2 σ, n = 22) (see Table A2). In addition, several international standards were run repeatedly, yielding results consistent with previous determinations (Table A3).

3.2 Li Concentration in Amphibole

To measure the Li concentration of amphiboles from amphibolites, laser ablation of thin sections and mounts were performed using the Element II single collector-ICP-MS coupled with a 213 nm wavelength laser at the University of Maryland. Multiple spots within a sample were measured using a spot size of 30-40 μm and ablation energy of 2-3 J/cm^2. The Li concentrations were calculated from two analyses of an external standard, NIST610 (CaO= 11.4 wt. %), run at the beginning and the end of each sample set of ≤ 16 analyses. The analysis of standard BCR-2g was undertaken to assess accuracy (see Table A4), which is within 9%. Data were processed using the LAMTRACE software. Li concentration uncertainties associated with the NIST610 standard vary from 0.1 % to 2.8 % (2σ).

To obtain an internal standard value for calculating Li concentration in amphiboles, major element compositions of amphiboles from the KX road cut were determined using the Electron Probe Microanalyzer (EPMA) at the University of Maryland. An accelerating voltage of 15 kV, a cup current of 20 nA, and a 10 μm beam were used for all the analyses. Raw X-ray counts were corrected using the ZAF algorithm. Calibration was performed using natural mineral standards. The results show that CaO content in amphiboles has little variation (multiple measurements of the same sample give 2σ < 0.9 %). Therefore, ^{43}Ca was chosen as the internal standard to correct for ablation yield in the amphiboles. Major element data are reported in Table A5.

3.2 Li in fluid inclusions and mineral separates from pegmatites

Fluid inclusions were extracted from quartz crystals of the KX pegmatite at the Central Michigan University by Mona-Liza Sirbescu and analyzed at the Geochemical Lab of the University of Maryland. Mineral separates from the ARA pegmatites are picked also by Mona. Then they were treated as whole rock samples and processed through column chemistry and instrumental analyses.

Chapter 4: Analytical Results

Lithium concentration and isotopic composition of the two profiles adjacent to the KX and ARA pegmatites and regional amphibolites/schists are reported in Tables 1 and 2. Li concentration of amphiboles in selected KX amphibolite country rocks are reported in Table 3 and plotted in Figure 7. The whole rock δ^7Li distribution of the KX profile is plotted in Figure 8. Whole rock lithium concentration and isotopic composition of the Animikie Red Ace profile are plotted against distance from the contact in Figures 9 and 10, respectively.

4.1 King-X Road Cut Profile

Li concentration of the only whole rock pegmatite sample is 31 ppm. This does not represent the Li content of the whole pegmatite because this sample is mainly composed of quartz and feldspar, which have very little Li compared to spodumene that is the main Li reservoir for the KX pegmatite. Li whole rock concentrations in the KX country rocks vary widely with distance away from the contact (Table 1). Nevertheless, almost all country rocks, except for three quartzites, have Li concentrations of more than 100 ppm. By contrast, lithium concentrations of the regional amphibolites and schists are much lower, roughly 20 ppm and 30 ppm, respectively. Despite the lack of systematics in whole rock Li concentration, Li contents of amphiboles in the KX amphibolite country rocks systematically decrease with distance away from the KX pegmatite (Figure 7).

Similar to Li concentration, the whole rock δ^7Li of the KX pegmatite sample, +10.2, is unlikely to represent the δ^7Li of the whole KX pegmatite, which should be dominated by the spodumene with a δ^7Li value of +1.5. In the country rocks, δ^7Li

decreases away from the contact on the left side of the KX pegmatite (Figure 8), -0.8 at ~ 0.15 m from the contact to ~ -8.0 in the farthest schist at ~ 10 m. On the right side of the KX contact, however, the trend in δ^7Li within the amphibolites is gentler and is accompanied by two humps: one is at ~5 to 10 m distance from the contact of KX, the other is from ~15 to 25 m from the contact. On this side of the pegmatite, the δ^7Li value shows a general decrease from +2 to +5 at the contact to ~ -7 in the farthest amphibolite at ~ 31 m. Interestingly, the LP quartz vein does not appear to influence the δ^7Li values of its surrounding country rocks.

Table 1. Li concentration and isotopic composition of whole rock samples in the KX and ARA pegmatites and country rocks.

Sample #	Rock Type	[Li] (ppm)	δ^7Li	Distance (m)
KingX Road Cut	Latitude: 45.85208°N	Longitude: 88.35409°W		
KX05	Schist	592	-7.8	-8.5
KX04(2)	Schist	426	-7.9	-6.5
KX03(2)	Schist	494	1.6	-3.2
KX02(2)	Schist	919	-0.8	-3.05
KX01	Pegmatite	31	10.2	-1.45
LP32	Schist	2618	5.0	0
LP33b(2)	Schist	1173	1.7	0
LP31	Schist	1307	4.2	0.5
LP30(2)	Amphibolite	56	-0.4	1.1
LP29(2)	Amphibolite	133	-1.1	2.5
LP28	Amphibolite	220	-0.2	3.3
LP27(2)	Quartzite	26	1.3	5.85
LP26(2)	Quartzite	58	0.2	9.25
LP25	Quartzite	53	1.7	10.8
LP25**	Quartzite	54	2.2	10.8
LP24	Amphibolite	706	-3.0	12.05
LP23	Amphibolite	232	-5.1	15.1
LP22	Amphibolite	136	-4.7	15.53
LP21	Amphibolite	158	-5.2	16.25
LP1(3)	Quartz vein	170	-0.5	16.47
LP2(2)	Amphibolite	238	-3.0	16.5
LP2*	Amphibolite	236	-4.3	16.5
LP3(2)	Amphibolite	69	-3.8	16.6

LP4[(2)]	Amphibolite	167	-4.0	16.7
LP4a[(2)]	Amphibolite	93	-2.9	17.17
LP4b[(2)]	Amphibolite	146	-3.9	17.65
LP5[(2)]	Amphibolite	112	-3.2	18.25
LP6[(4)]	Amphibolite	146	-2.3	19.25
LP10	Amphibolite	84	-2.3	21.3
LP9	Amphibolite	130	-3.4	23.5
LP8	Amphibolite	108	-5.6	26.3
LP7[(2)]	Amphibolite	102	-6.2	27.15
LP11	Amphibolite	149	-6.6	31.3
	Latitude:	Longitude:		
Animikie Red Ace	45.85013 °N	88.35120°W		
ARA1a[(3)]	Pegmatite 1	153	5.6	0
ARA1b[(2)]	Pegmatite 1	666	7.7	0
ARA2a[(2)]	Schist	484	4.2	0.1
ARA2b[(2)]	Schist	160	4.0	0.45
ARA2c[(2)]	Schist	297	4.7	1
ARA2d[(3)]	Schist	160	5.0	1.16
ARA2f[(2)]	Schist	197	5.3	1.55
ARA2e[(3)]	Schist	295	5.1	1.8
ARA2g[(2)]	Schist	243	6.2	2.7
ARA2h[(2)]	Schist	139	3.4	5.8
ARA2i[(2)]	Schist	287	1.1	10.9
ARA2j[(2)]	Schist	213	2.5	14
ARA2k[(2)]	Schist	106	-0.6	30
ARA2l	Amphibolite	148	-3.0	45.9
ARA2n	Amphibolite	116	-2.4	46.5
ARA2o	Amphibolite	89	-0.7	50.6
ARA2p	Amphibolite	180	-1.2	57.3
08-P-06	Pegmatite 2	167	7.0	60

Notes: [1] Lithium concentration is denoted as [Li] in this and the following tables. [2] External analytical uncertainties of [Li] and δ^7Li are $\leq \pm 10\%$ (2σ) and $\leq \pm 1$ (2σ), respectively. [3] "Distance" (the last column of the table) is the distance measured in meters away from the contact of a chosen pegmatite. In the KX profile, it is the distance from the KX right contact; in the ARA profile, it is the distance from the left ARA pegmatite (P1). [4] ** Redissolved and run through column chemistry from the same sample powder.
* Repeat column chemistry from same sample solution. [(#)]: Number of re-runs on ICP-MS from the same sample solution and values reported are therefore averages of all runs.

Table 2. Li concentration and isotopic composition of whole rock samples in regional amphibolites and schists.

Sample #	Rock Type	[Li] (ppm)	δ^7Li	Latitude	Longitude
QMA1	Amphibolite	19	2.8	45.8256°N	88.3404 °W
QMA2	Amphibolite	13	7.0	45.8256 °N	88.2881 °W
QMA2*	Amphibolite	17	6.3	45.8256 °N	88.2881 °W
QFM1	Schist	17	0.7	45.8516 °N	88.3404 °W
QFM3	Schist	23	1.3	45.8256 °N	88.2881 °W
QFM4	Schist	31	1.5	45.8256 °N	88.2881 °W
QFM5	Schist	51	-6.1	45.7763 °N	88.0566 °W
QFM5*	Schist	36	-6.1	45.7763 °N	88.0566 °W
QFM6	Schist	40	1.1	45.7763 °N	88.0566 °W

Note [1] * Repeat column chemistry from same sample solution.

Table 3. Li concentration of amphiboles in amphibolite country rocks.

Sample #	Mineral phase	[Li] (ppm)	2σ (ppm)	Distance (m)
LP2$^{(5)}$	Amphibole	226	54	16.5
LP6$^{(5)}$	Amphibole	142	40	19.25
LP8$^{(4)}$	Amphibole	144	26	26.3
LP21$^{(4)}$	Amphibole	234	68	16.25
LP26$^{(4)}$	Amphibole	268	106	9.25
LP30$^{(5)}$	Amphibole	363	66	1.1
LP10$^{(7)}$	Amphibole	147	32	21.3
LP11$^{(7)}$	Amphibole	79	28	31.3
LP29$^{(7)}$	Amphibole	282	64	12.05
QMA1$^{(12)}$	Amphibole	32	15	~ 1000

Notes: [1] Uncertainties are from two standard deviations of multiple measurements of each sample. Numbers of measurements are indicated as the superscripts $^{(\#)}$ of sample #. [2] "Distance" (the last column of the table) is the distance measured in meters away from the right contact of the KX pegmatite.

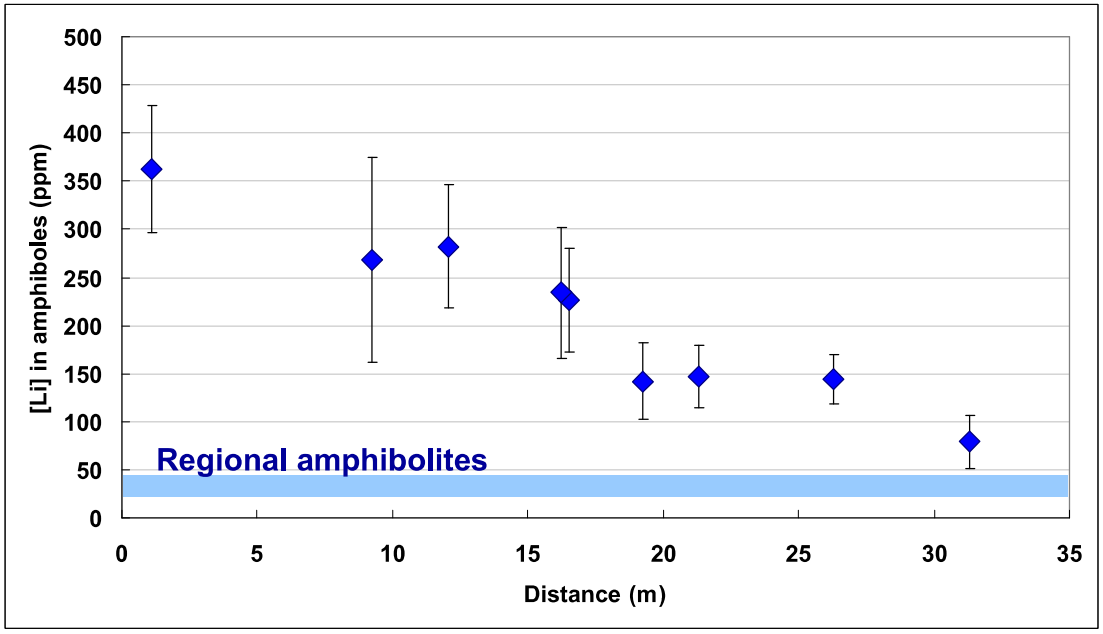

Figure 7. Plot of Li concentration of amphiboles in amphibolite from the KX Profile. Error bars associated are two standard deviations (2σ) calculated from multiple measurements of the sample. Data are from Table 3. Horizontal blue band represents Li concentration range in regional amphiboles.

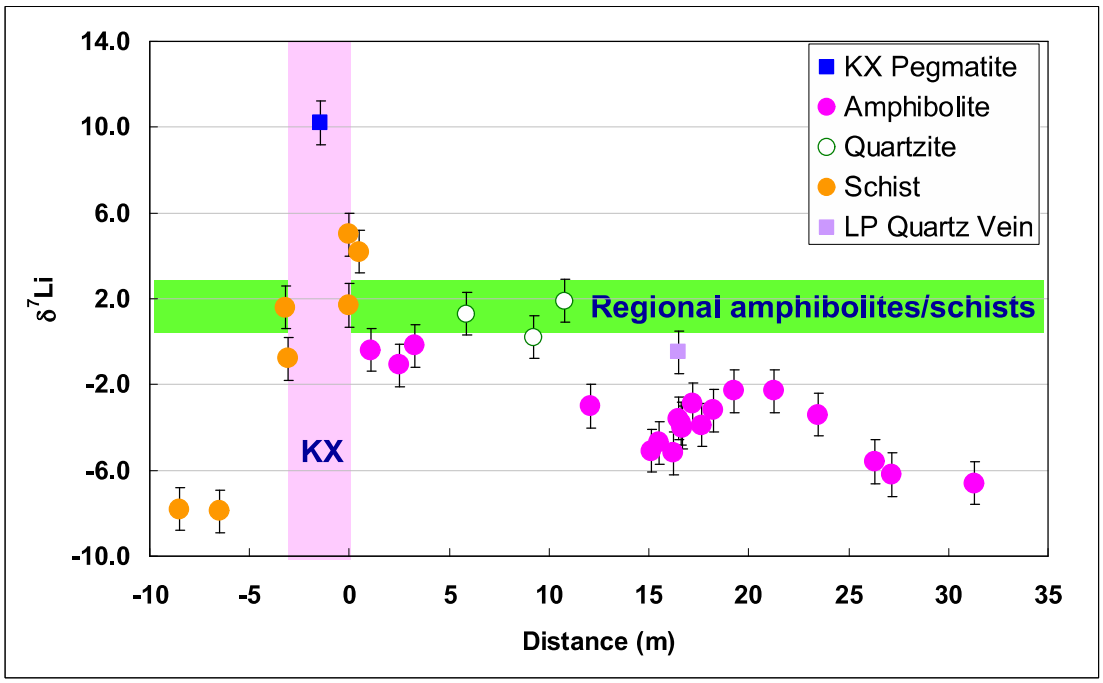

Figure 8. δ^7Li vs. distance from KX pegmatite contact. Data are from Table 1. Different rock types are denoted as symbols shown in the figure. Vertical pink band represents the KX pegmatite dike; horizontal green band indicates the δ^7Li range of regional schists and amphibolites, excluding two outliers.

4.2 Animikie Red Ace Profile

Li concentrations in the ARA pegmatites vary greatly. Two pegmatite samples, one quartz-rich and one tourmaline-rich from P1 have Li concentrations of 150 and 670 ppm, respectively. The pegmatite sample from P2 has a Li concentration of 170 ppm. In the ARA country rocks, Li concentrations decrease with distance away from the pegmatite (P1) contact up to ~ 30 m away (Figure 9). Closer to the P2 pegmatite, within the amphibolite, Li concentration does not show any obvious trend, but remains substantially higher than in the regional amphibolites.

The δ^7Li values in the ARA pegmatites do not vary significantly. The two P1 pegmatite samples have δ^7Li of +5.6 and +7.7, respectively. And the P2 pegmatite has δ^7Li of +7.0. Like the KX profile, δ^7Li in the ARA country rocks show a general decrease with distance away from the pegmatite (P1) contact, from ~ +4 and ~ +6 in the country rocks near the contact to -3.0 at ~ 45 m away from the P1 contact (Figure 10). The δ^7Li values then increase slightly towards the P2 pegmatite.

4.3 Regional Samples

Li concentrations in the regional schist and amphibolite samples range from ~17 ppm to 44 ppm and ~15 ppm to ~20 ppm, respectively, which are typical of published data for schists and amphibolites (Teng et al, 2004; 2006a). Except for two extreme values (-6.1 and +6.7), δ^7Li values in these regional schists and amphibolites range from +0.7 to +2.8, which is similar to typical upper crustal values (Teng et al., 2004). By contrast, the schist and amphibolite country rocks from both the KX and ARA profiles generally have greater than 100 ppm Li.

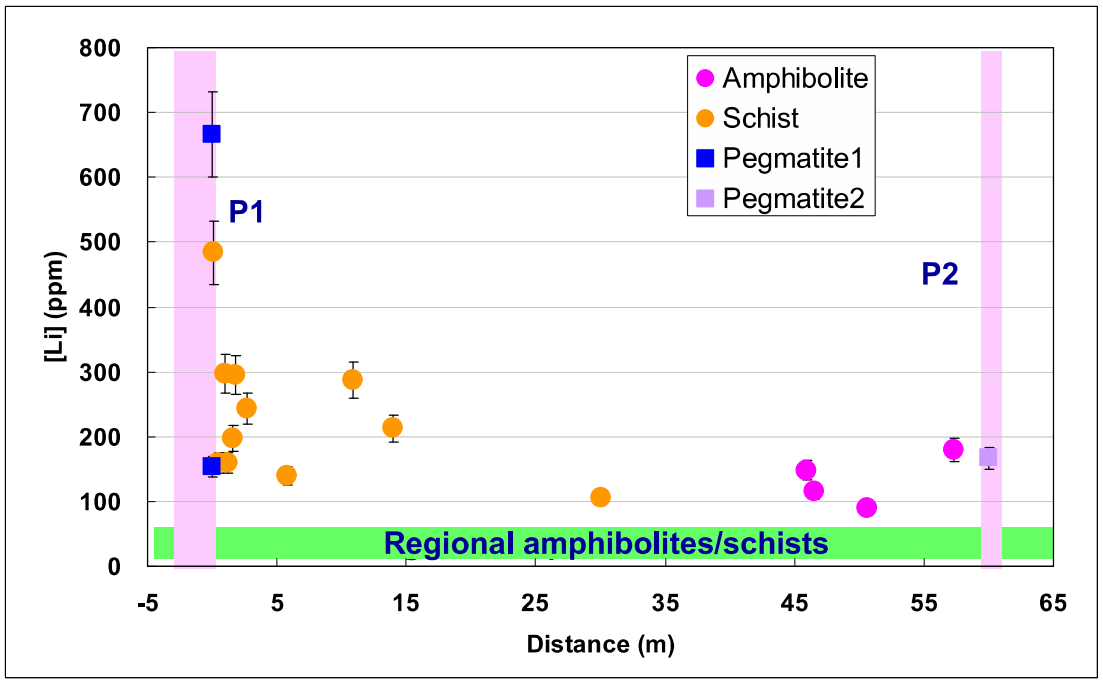

Figure 9. [Li] vs. distance away from Animikie Red Ace (ARA1) pegmatite contact. Data are from Table 1. Different rock types are denoted as symbols shown in this figure. Vertical pink bands represent the P1 and P2 pegmatite dikes; horizontal green band indicates the [Li] range of regional schists and amphibolites.

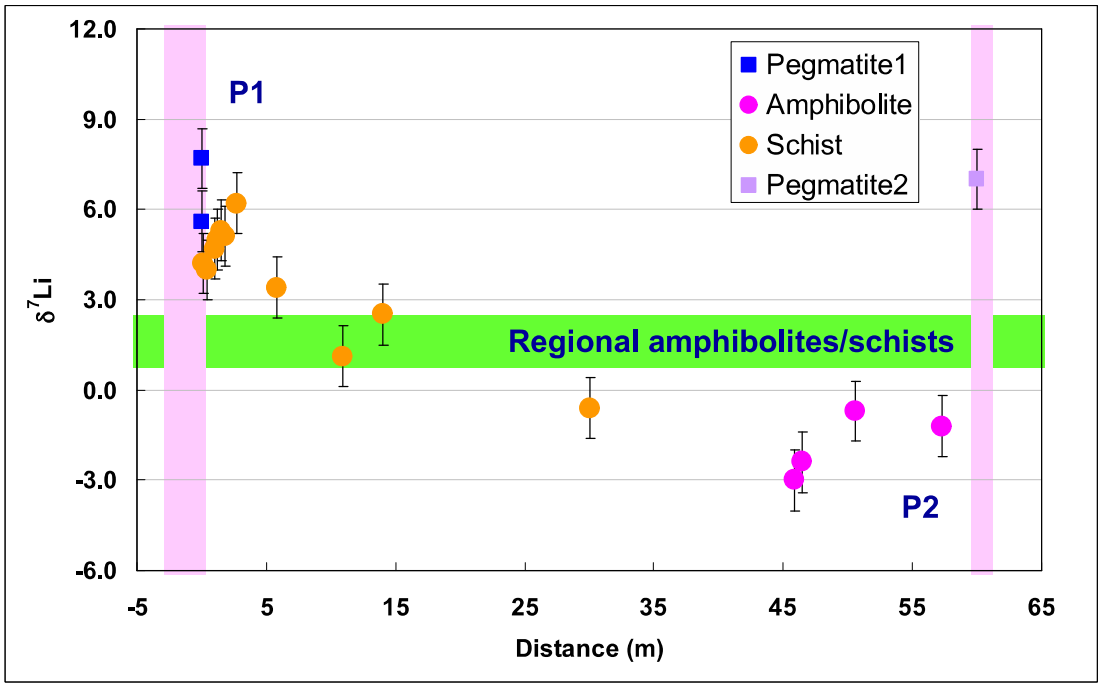

Figure 10. δ^7Li vs. distance for the Animikie Red Ace (ARA1) profile. Data are from Table 1. Different rock types are denoted as symbols shown in this figure. Vertical pink bands represent the P1 and P2 pegmatite dikes; horizontal green band indicates the δ^7Li range of regional schists and amphibolites.

4.4 Pegmatite Mineral Separates and Fluid Inclusions

Data for mineral separates and fluid inclusion leachates from the pegmatites are provided in Table 4. Li concentrations are plotted against δ^7Li in Figure 11.

Three fluid inclusion leachates from the ARA pegmatites show uniform and high δ^7Li values (+18.0 - +19.9). However, Li concentrations vary widely from 78 to 209 ppm.

Spodumene from the KX pegmatite has ~ 2 wt. % Li and δ^7Li of +1.5, which is significantly lower than that of the bulk pegmatite (+10.2). Tourmalines from the ARA pegmatites have variable Li concentrations from 415 to 3875 ppm, however, δ^7Li is within the analytical uncertainty, ranging from +6.1 to +8.2. Li concentrations in Li-rich micas of the ARA pegmatites range from 122 to 730 ppm, with a δ^7Li range of +2.0 to +8.0, showing a positive correlation between Li content and δ^7Li. In sum, different minerals from the ARA pegmatite have δ^7Li that varies well beyond the analytical uncertainty. Even single minerals (e.g., Li-rich micas) have variable δ^7Li.

Table 4. Li concentration and isotopic composition of mineral separates and fluid inclusion leachates.

Sample #	Type	[Li] (ppm)	δ^7Li
Fluid Inclusions Leachates (ARA Pegmatites)			
08-ARA-4B	Fluid inclusion	80	19.0
08-ARA-1C-1	Fluid inclusion	210	19.9
08-ARA-1C-2	Fluid inclusion	200	18.0
Mineral Separates from Pegmatites			
KX Pegmatite			
407-Db	Spodumene	22330	1.5
ARA Pegmatite			
ARA-1C-1	Tourmaline	420	7.0
ARA-1C-2	Tourmaline	1130	8.2
ARA-4b-1	Tourmaline	3880	6.1
ARA-1C-1	Li-rich micas	330	5.7
ARA-1C-2	Li-rich micas	730	8.0

ARA-4b-1	Li-rich micas	140	2.0
ARA-4b-2	Li-rich micas	120	2.6

Note: [1] All fluid inclusions are from quartz leachates in the ARA pegmatites. [2] Tourmalines and Li-rich micas are different grains from the ARA pegmatites and the spodumene is from the KX pegmatite.

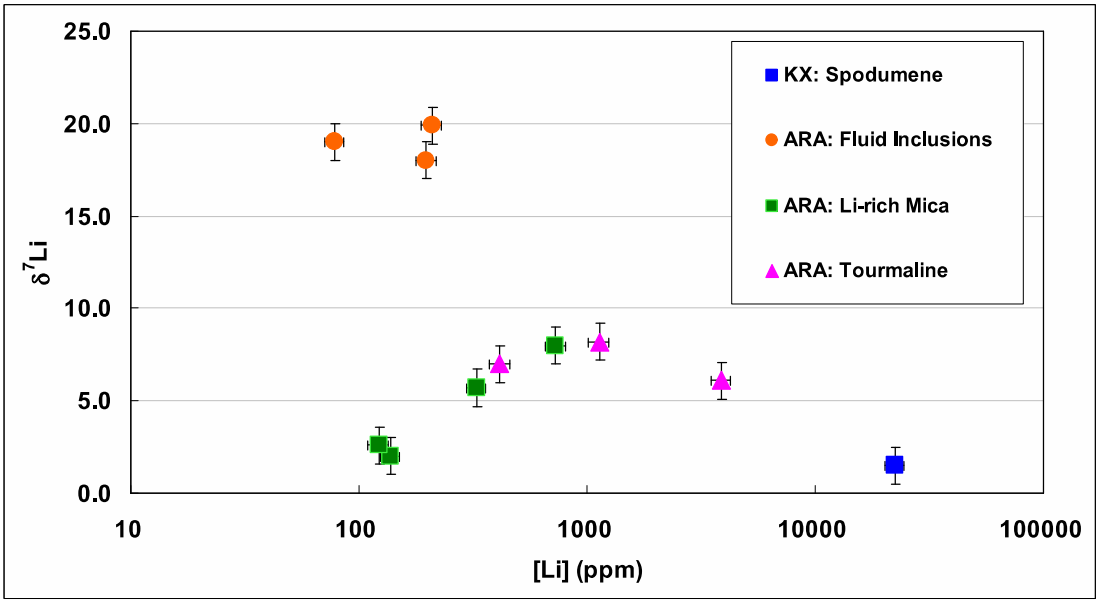

Figure 11. The KX pegmatite δ^7Li vs. [Li] (log-scale) plot for fluid inclusions and mineral separates.

Chapter 5: Numerical Modeling

The geochemical observations from the last chapter indicate that fluid infiltrates from the pegmatite intrusions into their adjacent country rocks. Percolation of Li-rich pegmatitic fluid through the country rock leads to the observed Li enrichment in the country rock compared to the regional samples. In addition, the δ^7Li distributions in country rocks indicate isotopic fractionation. Given the large Li concentration gradients between pegmatites and their country rocks, the Li isotopic fractionation is likely to be caused by differential chemical diffusion of the two Li isotopes.

In this chapter, I present the details of the numerical model of 2-D advection-diffusion transport of Li through the country rocks. I first present the model formulation and assumptions, then the governing equations and boundary conditions in sections 5.1 and 5.2, respectively. Next I discuss the details of nondimensionalization and parameter constraints on the numerical modeling in Section 5.3. Finally, numerical schemes are elaborated in Section 5.4.

5.1 Formulation and Assumptions

In this model, the chemical fingerprint of Li in the country rock is governed by advective-diffusive transport of Li in a percolating pore fluid. The percolation of the pore fluid is driven by pressure gradients and modulated by permeability, which depends on the lithology of the country rocks. The diffusion of Li isotopes is driven by the concentration gradient of Li in the pore fluid and the country rock. The 2-D two-phase fluid flow model simulates percolation of Li-rich fluid flow from vertical pegmatite dikes into their adjacent porous country rocks in a rectangular domain. The

fluid flow is driven by pressure gradients. The vertical pressure gradient is produced by the buoyancy difference between fluid and rock; while the horizontal pressure gradient is caused by the increase in pore pressure triggered by intrusion of pegmatites into the fluid-saturated country rocks (Ferry, 1994 and references therein).

The model geometry is displayed in Figure 12 for the KX profile (11A) and the ARA profile (11B). Although the influence of the smaller pegmatite (P2) observed in the ARA profile is apparently smaller than the larger pegmatite (P1), both intrusions are considered in the model. In the following formulation, the porous country rock is referred to as the solid.

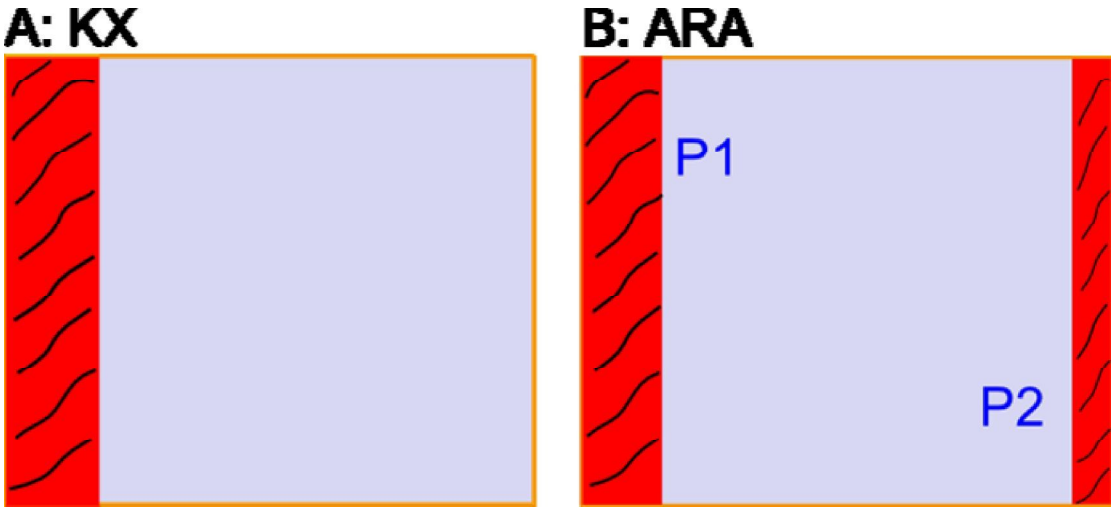

Figure 12. Model geometry of King-X (KX) and Animikie Red Ace (ARA) profiles. Pegmatite intrusions are shown in red. The blue rectangular fields are their adjacent country rocks of the model fields.

To simplify the numerical modeling, the following assumptions are made:

1. No phase change occurs between fluid and solid.
2. No temperature gradient exists between the pegmatites and their country rocks.
3. Diffusion coefficients of ^{7}Li and ^{6}Li are constant.
4. The porosity of the country rocks is constant.
5. Permeability is constant in the country rocks.
6. There is zero motion of solid.

7. There is no shear stress in either solid or fluid.
8. Li distributions in the country rocks reached steady-state.
9. In the case of the ARA profile, two pegmatite dikes intruded simultaneously.

5.2 Governing Equations and Boundary Conditions

Percolation of a physically and chemically distinct fluid phase through a porous matrix is governed by coupled mass and momentum conservation of both the fluid and the matrix phases. These governing equations of two-phase viscous flow are presented in a number of studies (e.g., Bercovici et al., 2001; Connolly and Podladchikov, 1998; Drew and Passman, 1999; Hier-Majumder et al., 2006; McKenzie, 1984; Ricard et al., 2001; Richter and McKenzie, 1984; Scott and Stevenson, 1984).

In the absence of melting, the equation for the mass conservation for the fluid is given by

$$\frac{\partial \varphi}{\partial t} + \nabla \cdot (\varphi \mathbf{V}_f) = 0 , \qquad (1)$$

where φ is the volume fraction of the fluid (here defined as the same value as porosity), $\mathbf{V}_f$ is the fluid flow velocity, t is time (see Table 5 for a list of all symbols used).

Similarly, the mass conservation for the solid yields

$$\frac{\partial (1-\varphi)}{\partial t} + \nabla \cdot [(1-\varphi)\mathbf{V}_s] = 0 , \qquad (2)$$

where $\mathbf{V}_s$ is the velocity of the solid.

In this work, I assume there is no motion of the solid ($\mathbf{V}_s$=0) and the volume fraction of fluid φ is constant. Therefore, we can simplify equations (1) and (2) to

$$\nabla \cdot (\mathbf{V}_f) = 0 . \qquad (3)$$

Momentum conservation for the fluid and solid are

$$-\varphi\nabla P_f - \varphi\rho_f \boldsymbol{g} - \eta_f \varphi^2 \underline{\underline{\mathbf{K}}}^{-1} \cdot \mathbf{V}_f = 0 \qquad (4)$$

$$-(1-\varphi)\nabla P_s - (1-\varphi)\rho_s \boldsymbol{g} + \eta_f \varphi^2 \underline{\underline{\mathbf{K}}}^{-1} \cdot \mathbf{V}_f = 0\,, \qquad (5)$$

where P_f and P_s are the fluid and solid pressure, respectively, ρ_f and ρ_s are the density of the fluid and rock, respectively, $\boldsymbol{g}$ is the gravitational constant, η_f is the dynamic viscosity of the fluid, and $\underline{\underline{\mathbf{K}}}$ is the permeability tensor in the solid. Permeability is defined as the capacity of a material to transmit fluids, modulating the flow fluid. In equations (4) and (5), the first term, (containing pressure of fluid/solid), represents the pressure gradient within the fluid and solid; the second term is the buoyancy caused by the gravitational force, and the last term (containing the permeability $\underline{\underline{\mathbf{K}}}$), is the drag force between fluid and solid, which has the same magnitude and opposite directions. Thus, the percolation of the pore fluid is determined by forces arising from pressure, buoyancy, and interfacial friction.

Multiplying equation (4) by (1- φ) and subtracting from equation (5) multiplied by φ, we obtain

$$(1-\varphi)\nabla(\Delta\overline{P}) + \eta_f \varphi \underline{\underline{\mathbf{K}}}^{-1} \cdot \mathbf{V}_f = 0\,, \qquad (6)$$

where $P_s - P_f = \Delta P$, $\Delta\overline{P} = \Delta P + \Delta\rho g y$ and $\rho_s - \rho_f = \Delta\rho$. The pressure gradient is the driving force of the fluid flow.

To eliminate $\mathbf{V}_f$ from the governing equations, we take the divergence of equation (6) and substitute $\nabla\cdot(\mathbf{V}_f)$ from equation (3), yielding

$$\nabla\cdot(\underline{\underline{\mathbf{K}}}^{-1}\cdot\nabla\overline{P}) = 0\,. \qquad (7)$$

Once the value of $\Delta\overline{P}$ is obtained by solving equation (7), we can use another form of equation (6):

$$\mathbf{V}_f = -\frac{\underline{\underline{\mathbf{K}}} \cdot \nabla(\Delta\overline{P})}{\eta_f}\left(\frac{1-\varphi}{\varphi}\right) \qquad (8)$$

to solve for $\mathbf{V}_f$. Equation (8) is basically another form of Darcy's law of fluid flow, which states that the fluid flow velocity is proportional to the pressure gradient (e.g., McKenzie, 1984).

The diffusion and mass conservation equation for ^{6}Li and ^{7}Li are:

$$\frac{\partial(C^6)}{\partial t} + \nabla \cdot (C^6 \mathbf{V}_f) = D^6 \nabla \cdot (\nabla C^6) \qquad (9)$$

$$\frac{\partial(C^7)}{\partial t} + \nabla \cdot (C^7 \mathbf{V}_f) = D^7 \nabla \cdot (\nabla C^7) \qquad (10)$$

where C^6 and C^7 are the concentrations of ^{6}Li and ^{7}Li in the fluid, respectively, D^6 and D^7 are the diffusion coefficients for ^{6}Li and ^{7}Li, respectively, and $\nabla \cdot (C^i \mathbf{V}_f)$ and $D^i \nabla^2 C^i$ (i = 6 or 7) are advection and diffusion terms, respectively.

Under steady-state conditions ($\frac{\partial C^i}{\partial t} = 0$) and the assumption that diffusion coefficients are constant, equations (9) and (10) can be simplified to

$$\nabla \cdot (C^6 \mathbf{V}_f) = D^6 \nabla^2 C^6 \qquad (11)$$

$$\nabla \cdot (C^7 \mathbf{V}_f) = D^7 \nabla^2 C^7 \qquad (12)$$

Then we can use equations (11) and (12) to calculate lithium isotopes concentration and isotopic composition.

Table 5. Symbols used in text.

Symbols	Name of Parameters	Units
φ	Porosity	N.U.
t	Time	s
$\mathbf{V_f}$	Fluid velocity	m/s
$\mathbf{V_m}$	Solid velocity	m/s
P_f	Fluid pressure	Pa
P_m	Solid pressure	Pa
ΔP	Pressure difference between solid and fluid	Pa
ρ_f	Density of fluid	kg/m^3
ρ_m	Density of solid	kg/m^3
$\Delta\rho$	Density difference between solid and fluid	kg/m^3
g	Gravitational constant	m/s^2
η_f	Dynamic viscosity of fluid	Pa s
$\underline{\underline{\mathbf{K}}}$	Permeability tensor	m^{-2}
y	Depth	m
C^6	Concentration of ^{6}Li	ppm
C^7	Concentration of ^{7}Li	ppm
D^6	Effective diffusion coefficient of ^{6}Li	m^2/s
D^7	Effective diffusion coefficient of ^{7}Li	m^2/s
$\mathbf{V_f}^*$	Dimensionless fluid velocity	N.U.
t^*	Dimensionless time	N.U.
D^*	Dimensionless effective diffusion coefficient	N.U.
P^*	Dimensionless total pressure	N.U.
$\underline{\underline{\mathbf{K}}}^*$	Dimensionless permeability tensor	N.U.
K	Magnitude of permeability tensor	m^2
L	Characteristic length	m
V_o	Magnitude of fluid velocity	m/s
D_o	Magnitude of effective diffusion coefficient of ^{7}Li	m^2/s
Pe	Peclet number	N.U.
D^{*6}	Dimensionless effective diffusion coefficient of ^{6}Li	N.U.
D^{*7}	Dimensionless effective diffusion coefficient of ^{7}Li	N.U.
z	Depth	km
m^7	Atomic weight of ^{7}Li	N.U.
m^6	Atomic weight of ^{6}Li	N.U.
β	Empirical parameter determined experiments	N.U.

Note: [1] N.U. = dimensionless or no unit. [2] The order of symbol arrangement is from the order of appearance in the text.

Both vertical pressure and horizontal pressure are imposed at the boundaries of the rectangular domain. A linearly varying pressure with depth is imposed at both left and right boundaries. At the KX profile, an extra constant is added to the linearly

varying pressure with depth at the left boundary, simulating the increased pressure triggered by the intrusion of the KX pegmatite that drives Li-rich fluids into the fluid-saturated country rocks. For the ARA profile, two different constants are added to the linearly varying pressure with depth at both left and right boundaries, accounting for the increased pressure triggered by two pegmatite intrusions at the left and right of the ARA modeling domain. The pressure at the top boundary is prescribed to be zero and the pressure at the bottom boundary is the same as the bottom value of the left boundary. For consistency, this value is the same in both the KX and ARA profiles.

The top and bottom concentration boundary conditions for the country rocks are taken from the average concentrations of the regional schists and amphibolites samples (27 ppm). In the case of one pegmatite intrusion, as in the KX profile, the single pegmatite whole rock analysis (31 ppm Li) is clearly too low to represent the true pegmatite concentration. Instead, a Li concentration of 400 ppm in the KX pegmatite is used as the left boundary condition in the modeling, because Li concentration of amphibole in amphibolite (1.1 m) from the nearest KX contact is 363 ppm. This concentration is most likely to be a minimum value for the pegmatites since the pegmatites are composed of Li-rich minerals (e.g., tourmaline and spodumene), which control the Li budget in pegmatites and their country rocks. The right concentration boundary is based on the Li concentration in the farthest country rocks (~32 m) from the contact (79 ppm). For the ARA profile, where two pegmatites intruded at the left and right boundary of the modeling domain, Li concentrations of 500 ppm and 200 ppm at the left and right boundaries are used for the modeling because Li concentration in the nearest schist (0.1 m) from the P1 contact is 484 ppm and the nearest amphibolite country rock (2.7 m) from the P2 contact is 180 ppm. As

will be shown in the next Chapter, the choice of Li concentrations at the boundary does not influence Li distributions much in either profile.

Boundary conditions for pressure, concentration and δ^7Li of the KX and the ARA profiles are displayed in Figure 13.

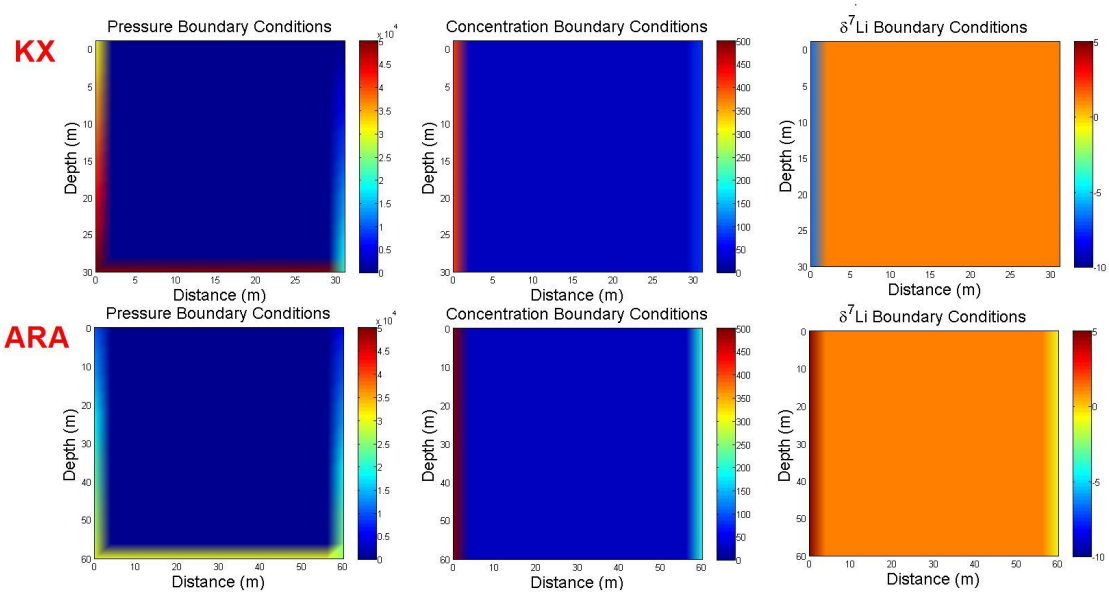

Figure 13. Boundary conditions of the KX and ARA profiles for pressure (left panel), [Li] (middle panel), and δ^7Li (right panel). A linearly varying pressure is assigned with increasing depth, providing a constant vertical pressure gradient. [Li] and δ^7Li boundary conditions for the KX and ARA profiles are the same as discussed above. Pressure unit is Pa, and concentration unit is ppm.

Besides pressure and Li concentration boundary conditions, the ratios between ^{7}Li and ^{6}Li, expressed as δ^7Li, at the boundaries of the modeling domains are also assigned to solve Li concentration and δ^7Li distributions numerically. Similar to the Li concentration boundary conditions, the top and bottom δ^7Li boundary conditions for the country rocks are also taken from the average concentrations of the regional schists and amphibolites samples (+1.2). For the KX profile, at the right contact (0 m) of the KX pegmatite, two samples give different δ^7Li values of +1.7 and +5.0, respectively. However, the spodumene mineral separate from the KX pegmatite gives a δ^7Li value of +1.5 and we know that spodumene is the main Li reservoir in the KX

pegmatite. Therefore, the left boundary is from the δ^7Li of the spodumene, +1.5, and the right boundary, -6.6, is from the farthest amphibolite (31.3 m) from the KX contact. For the ARA profile, δ^7Li of +5.0 and -1.0 at the left and right boundaries are used in the numerical modeling because δ^7Li in the nearest schist (0.1 m) from the P1 contact is +4.2 and the nearest amphibolite country rock (2.7 m) from the P2 contact is -1.2. Like the Li concentration, the choice of δ^7Li at the boundary does not influence Li elemental and isotopic distributions much in either profile.

5.3 Nondimensionalization

Parameters used in nondimensionalization are as follows (the dimensionless parameters are denoted with an asterisk):

$$\mathbf{V}_f = V_o \mathbf{V}_f^*$$
$$t = \frac{L}{V_o} t^*$$
$$\nabla = \frac{1}{L} \nabla^*$$
$$\nabla \bar{P} = \Delta\rho g \nabla^* \bar{P}^*$$
$$D = D_o D^*$$

where V_o is the magnitude of the fluid advection velocity, expressed as $V_o = \frac{K\Delta\rho g}{\eta_f}\left(\frac{1-\varphi}{\varphi}\right)$, and L is the characteristic length, which represents the length scale of the advection process. The corresponding time scale of the advection process is t. The magnitude of the pressure gradient is $\Delta\rho g$ and the magnitude of the ^{7}Li diffusion coefficient is equal to D_o.

The nondimensionalized forms of the above governing equations are

$$\nabla \cdot (\underline{\underline{\mathbf{K}}}^{*-1} \cdot \nabla^* \bar{P}^*) = 0 \qquad (13)$$

$$\mathbf{V}_f^* = -\underline{\underline{\mathbf{K}}}^* \cdot \nabla^* \bar{P}^* \qquad (14)$$

$$Pe\nabla^* \cdot (C^6 \mathbf{V}_f{}^*) = D^{*6}\nabla^{*2} C^6 \qquad (15)$$

$$Pe\nabla^* \cdot (C^7 \mathbf{V}_f{}^*) = \nabla^{*2} C^7 . \qquad (16)$$

where *Pe* is the Peclet number, which is the ratio of the magnitude of advection to diffusion, mathematically defined as

$$Pe = \frac{V_o L}{D_o} = \frac{K\Delta\rho g L}{\eta_f D_o}\left(\frac{1-\varphi}{\varphi}\right). \qquad (17)$$

Equations (13)-(16) need to be solved numerically and then redimensionalized according to the magnitude of the nondimensionalized parameters. To determine the values of these parameters, we need to adopt values for the porosity and permeability of the country rock, vertical pressure gradient, characteristic length, dynamic viscosity of fluids in porous rocks and effective diffusion coefficients of Li isotopes. These parameters are discussed below.

The permeability of porous rocks is dependent on their depths. Manning and Ingebritsen (1999) suggest the following permeability and depth relationship, after considering the permeability values inferred from thermal modeling and metamorphic systems: $\log K \approx -3.2\log(z)-14$, where z is depth in km and K is the corresponding permeability in m^2. Thus, if we assume a pegmatite intrusion depth of ~10-11 km, we obtain an estimated permeability of $10^{-17.2}$ m^2. Considering the uncertainty of the relationship, a permeability range of 10^{-16}~10^{-18} m^2 is adopted here for estimating the value of the Peclet number. In addition, foliation is a primary source of anisotropy for permeability in metamorphic rocks. Hueng et al. (1997) suggest that permeability parallel to foliation is up to an order of magnitude larger than permeability perpendicular to the foliation within the same rocks.

The estimated porosity of the country rocks are taken from Connolly (1997), who found 10^{-3} to 10^{-4} based on modeling of metamorphism in a contact aureole. This

range is used for the calculation of the Peclet number in the numerical modeling.

The characteristic length is determined according to the scale of modeling domain. For example, the characteristic length is ~ 60 m in the ARA profile, which is the observed distance between the two pegmatites.

Dynamic viscosity is a measure of resistance of a fluid deformed by either shear or extensional stress. A representative value of dynamic viscosity of water at ~10 km is ~1.5×10^{-4} Pa s (Walther and Orville, 1982). The dynamic viscosity of fluids in porous rocks, η_f, should have a similar value.

Currently, there is no direct measurement of effective Li diffusion coefficient in porous metamorphic rocks. However, Teng et al. (2006a) estimate a minimum of 2×10^{-8} m^2/s for grain boundary diffusion of Li in amphibolite country rocks from the Tin Mountain pegmatite. They also found that the effective Li diffusion coefficient is ~10 times larger in schist compared to the value in amphibolite country rocks. Thus, the value 1×10^{-7} m^2/s is used to estimate the Peclet number.

^{6}Li and ^{7}Li diffuse at different rates. According to Richter et al. (1999), the ratio of the effective diffusion coefficients of the isotopes ^{6}Li and ^{7}Li are as follows: $\frac{D^6}{D^7}=\left(\frac{m^7}{m^6}\right)^{\beta}$, where β is an empirical parameter to be determined from experimental data and m^7 and m^6 are the atomic masses of ^{6}Li and ^{7}Li. Richter et al. (2003) found β is 0.215 for Li diffusion between basalt and rhyolite melts. For water, β is considered to be low, 0.015 to 0.071 from Richter et al. (2006) and Fritz (1992), respectively. β in our system of porous rocks should be between Li diffusion in water and melt. Teng et al. (2006a) found a best fit β of 0.12 based on 1-D diffusion in amphibolite country rocks. I therefore adopt this value here, but investigate the effects of allowing β to vary from 0.02 to 0.2 in the next chapter.

Combining the parameters given above with the estimation of the difference between the lithostatic and hydrostatic gradients $\Delta\rho g = \sim 1.7\times10^{4}$ - 2.0×10^{4} Pa m^{-1} (Ague, 2003), the estimated Peclet number ranges from ~ 1 to 100. The diffusion only case, where the Peclet number is equal to zero, is also considered in the modeling.

5.4 Numerical Scheme and Coding

The numerical scheme adopted in this modeling is the finite volume method. The discretization scheme is similar to that described in Patankar (1980), which uses the five-point stencil scheme and is attached in Appendix A. The numerical modeling was performed using Matlab® as the coding language. The Matlab® codes of different solvers are attached in Appendix B. In addition, numerical solvers, including the Laplace solver of the pressure, advection-diffusion equations, and 1-D diffusion equations are attached in Appendix C as the validation of codes and compared with their corresponding analytical solutions. The maximum grid size used is 80×80 in a rectangular modeling domain.

Chapter 6: Modeling Results

In this chapter, the results of the 2-D fluid flow advection-diffusion models are presented for both the KX and ARA profiles, following the numerical methods described in Chapter 5. In addition, the influence of different parameters is evaluated. Two numerical cases were performed in this chapter: [1] KX profile, [2] ARA profile. Boundary conditions and parameters used in these models are displayed in Table 6 and MATLAB® codes of pressure, velocity and concentration solvers are attached in Appendix B.

The procedure for each case is as follows: Pressure profiles are solved based on prescribed horizontal and vertical pressure gradients at the boundaries in modeling domains. Velocity profiles are then solved using the pressure distribution. ^{7}Li and ^{6}Li are then treated as two different elements, and solved separately from advection-diffusion concentration solvers. Finally, Li concentration and $\delta^{7}Li$ profiles are calculated.

Table 6. Boundary conditions and parameters in different cases.

Profile	Pressure (Pa)	[Li] (ppm)	$\delta^{7}Li$	Peclet #	Beta	Grids
KX	$P_L=2\times10^4(x+1.5)$	$C_L=400$	$(\delta^{7}Li)_L=+1.5$	5.0	0.12	70×70
	$P_R=2\times10^4x$	$C_R=79$	$(\delta^{7}Li)_R=-6.6$			
	$P_T=0$ Pa, $P_B=5\times10^4$	$C_T=C_B=27$	$(\delta^{7}Li)_T=(\delta^{7}Li)_B=+1.2$			
ARA	$P_L=2\times10^4(x+0.5)$	$C_L=500$	$(\delta^{7}Li)_L=+5.0$	2.5	0.12	80×80
	$P_R=2\times10^4(x+0.03)$	$C_R=200$	$(\delta^{7}Li)_R=-1.0$			
	$P_T=0$ Pa, $P_B=3\times10^4$	$C_T=C_B=27$	$(\delta^{7}Li)_T=(\delta^{7}Li)_B=+1.2$			

Notes: [1] P and C are pressure and Li concentration, respectively. [2] Subscripts L, R,T, and B represent left, right, top, and bottom boundary of parameters. x ranges from 0 (top) to 1 (bottom). [3] Grids indicates how many grids exist in the 1×1 2-D modeling domain.

6.1 King-X Road Cut Profile

Pressure, velocity, Li concentration and δ^7Li profiles for country rocks adjacent to the KX pegmatite intrusions are shown in Figure 14.

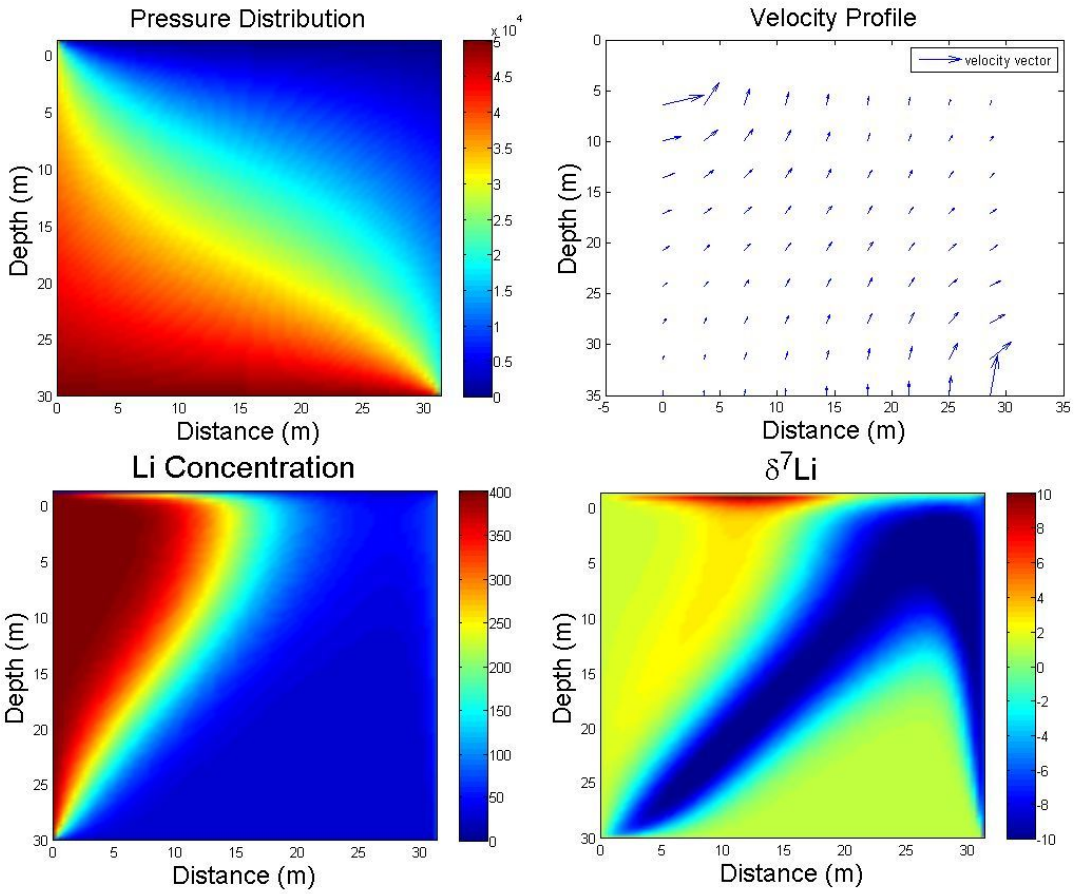

Figure 14. 2-D modeling results of steady-state KX distribution with constant permeability. Upper-left panel: Pressure distribution (unit is Pa). Upper-right panel: Velocity field. Lower-left panel: Li concentration distribution (unit is ppm). *Pe*=5.0. Lower-right panel: δ^7Li distribution (unit is ‰). β =0.12. Grids: 70× 70.

The pressure distribution solved in the constant permeability case shows increasing vertical pressure as depth increases and a horizontal pressure gradient from the pegmatite intrusion into the country rock. In the velocity distribution, boundary effects are prominent at the upper-left and lower-right corners of the modeling domain due to the large pressure gradients induced by the boundary conditions. Except for the regions that are close to the boundaries, however, the velocity distribution displays a strong vertical fluid flow due to fluid buoyancy and a relatively weaker horizontal

fluid flow from the pegmatite on the left boundary to the country rock. Thus, caution needs to be taken when examining the distributions in the areas close to upper and bottom boundaries. Concentration and δ^7Li distributions solved from the corresponding pressure and velocity field show Li concentration and isotopic composition distribution of the contact aureole at steady-state conditions.

6.2 Animikie Red Ace Profile

Pressure, velocity, Li concentration and δ^7Li distributions for country rocks adjacent to the ARA pegmatite intrusions are shown in Figure 15.

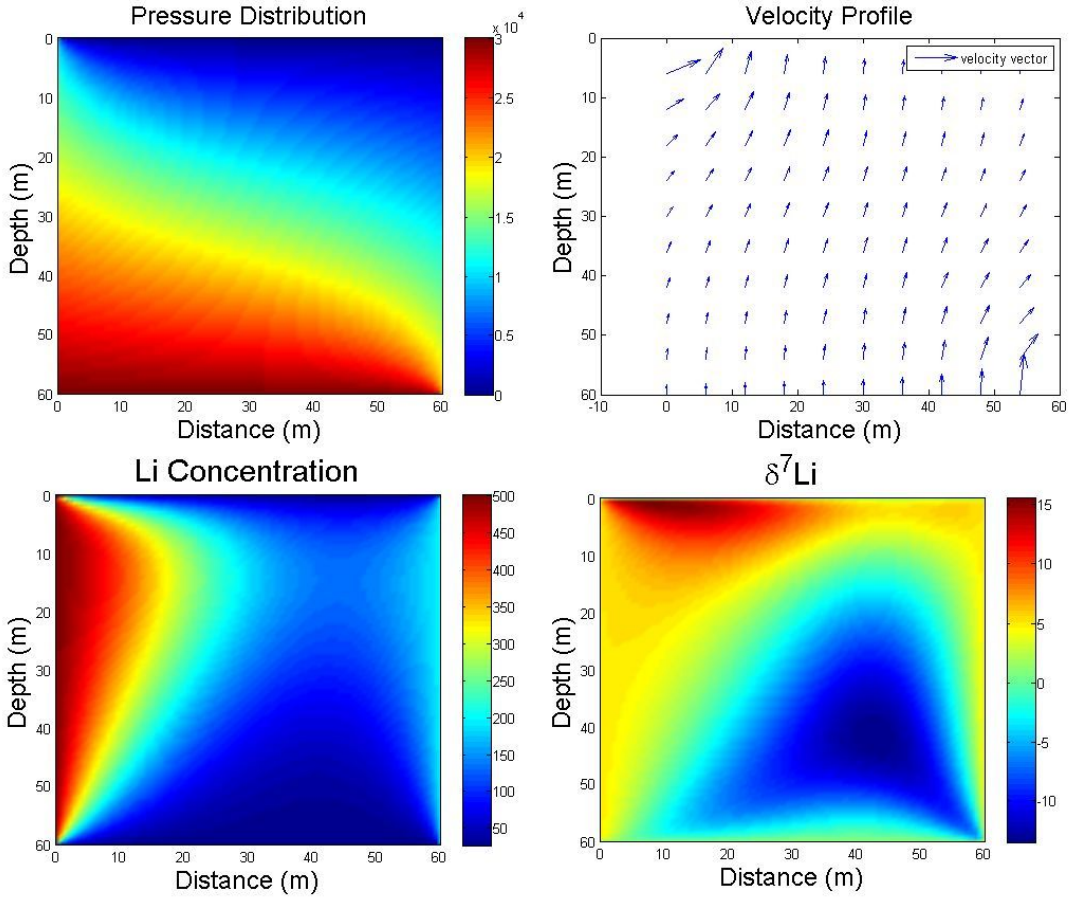

Figure 15. 2-D modeling results of steady-state ARA distribution with constant permeability. A. Pressure distribution (unit is Pa). B. Velocity field. C. Li concentration distribution (unit is ppm). *Pe*=2.5. D. δ^7Li distribution (unit is ‰). β =0.12. Grids: 80× 80.

The pressure distribution shows an increasing vertical pressure with increasing depth and different horizontal pressure gradients from two pegmatite intrusions into

the country rocks. Theoretically, the velocity distribution displays vertical fluid flow due to fluid buoyancy and horizontal fluid flow from the pegmatites on both left and right boundaries to the center of the country rock domain. However, the influence of the left pegmatite is much larger compared to the right one (Table 6). Therefore, the velocity vectors at the right show fluid flow direction from the left to right instead of the reverse direction. Similar to the KX profile, numerical artifacts are prominent at the upper-left and lower-right corners of the modeling domain due to the prescription of boundary conditions and caution then needs to be taken when examining the distributions at these areas. Concentration and δ^7Li distributions solved from the corresponding pressure and velocity field are all shown at steady-state conditions. All distributions show that the influence of the pegmatite on the left (P1) is greater than the pegmatite on the right (P2) because a stronger pressure gradient is prescribed to the P1 pegmatite under the assumption that P1 and P2 intruded simultaneously, and the exposure widths of the pegmatites track pressure gradients (P1 is about four times wider than P2).

6.3 Controlling Parameters

A prime objective of this study is to offer some insights on the most important parameters controlling Li elemental and isotopic distribution in metamorphic contact aureole settings. From equation (17) in Chapter 5, we know the Peclet number includes many parameters, such as porosity and permeability of the country rock, vertical pressure gradient, characteristic length, dynamic viscosity of fluids in porous rocks and effective diffusion coefficients of Li isotopes. Thus, the Peclet number alone reflects the balance between these parameters. Below, the influence of the Peclet number, β value, Li concentration and δ^7Li boundary conditions in this 2-D advection-diffusion modeling are investigated.

The Peclet number is an important parameter that controls Li distribution in contact aureoles and it ranges from 1 to 100 as estimated in Chapter 5. The effect is well illustrated in Figure 16, where all modeling parameters are held constant except for the Peclet number. The upper and lower panels of Figure 16 show very different Li distribution in the KX right contact, with Pe = 1 and 100, respectively. With larger Peclet number (Pe = 100), Li concentrations are elevated at greater distance away from the contact and then drop dramatically. Also, δ^7Li shows relatively smoother distributions compared to the lower Peclet number case (Pe = 1). β defines the degree of the fractionation between ^{7}Li and ^{6}Li during diffusion. As discussed in the previous chapter, β may vary from 0.02 to 0.22 during fluid-assisted grain boundary diffusion. The effect of varying β is shown in Figure 17, where Li concentrations in the two extreme case (β=0.02 and 0.22) does not show an obvious change. By contrast, δ^7Li distributions show more obvious change, in the case of β=0.22, δ^7Li shows larger change, as expected because of the increased isotopic fractionation between ^{7}Li and ^{6}Li at higher β.

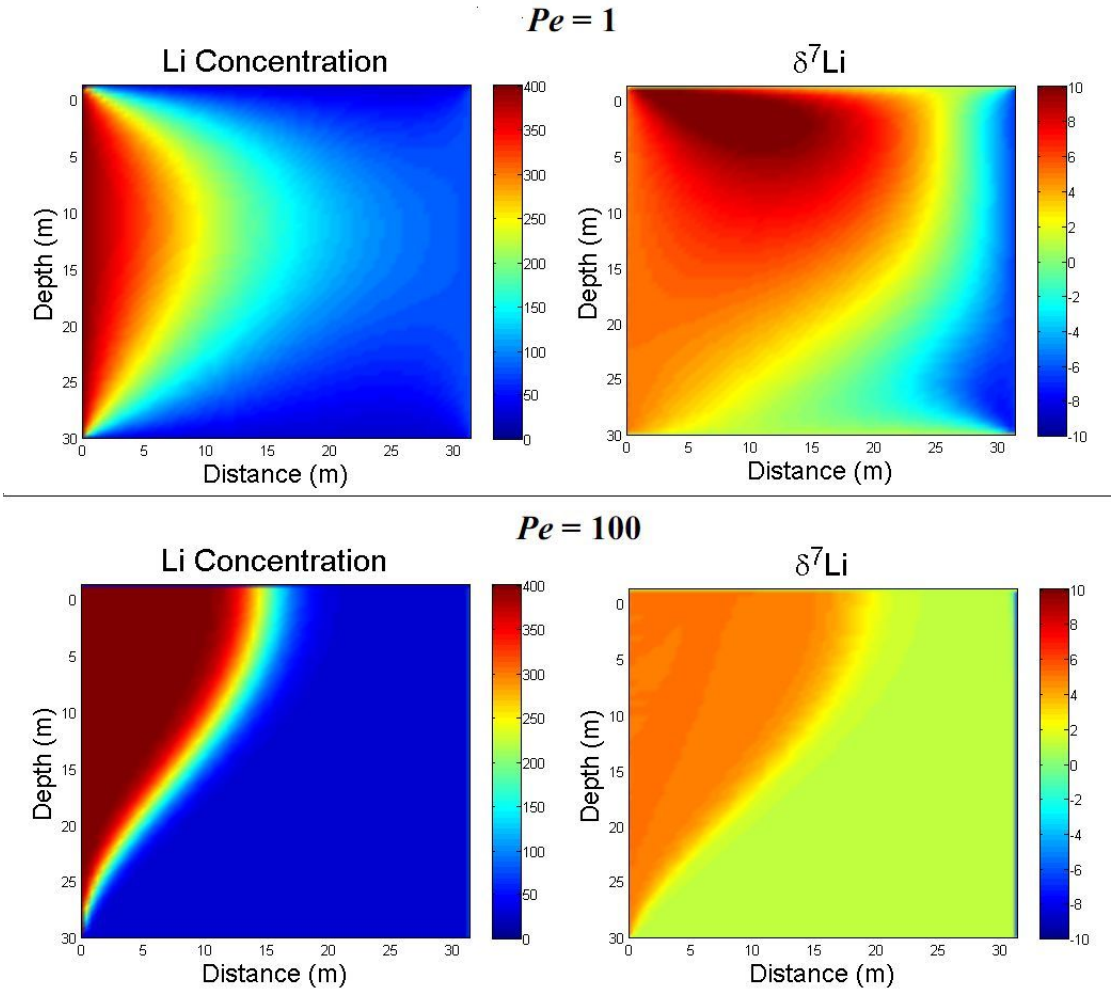

Figure 16. The influence of *Pe* on model outcomes for [Li] (left panels) and δ^7Li (right panels) distribution. In all models, β=0.12, C_L=400 ppm, and δ^7Li=+5.

In contrast to Peclet number and β, changing Li concentration and δ^7Li at the boundaries of the model within reasonable bounds do not significantly influence the δ^7Li distributions. For example, the lower panel of Figure 18 shows what happens when the Li concentration at the left boundary (KX contact) is increased by a factor of two. The pattern of Li concentration and δ^7Li distributions are virtually unchanged. Similarly, Figure 19 shows that changing δ^7Li at the KX by a factor of two produces no significant change in the results.

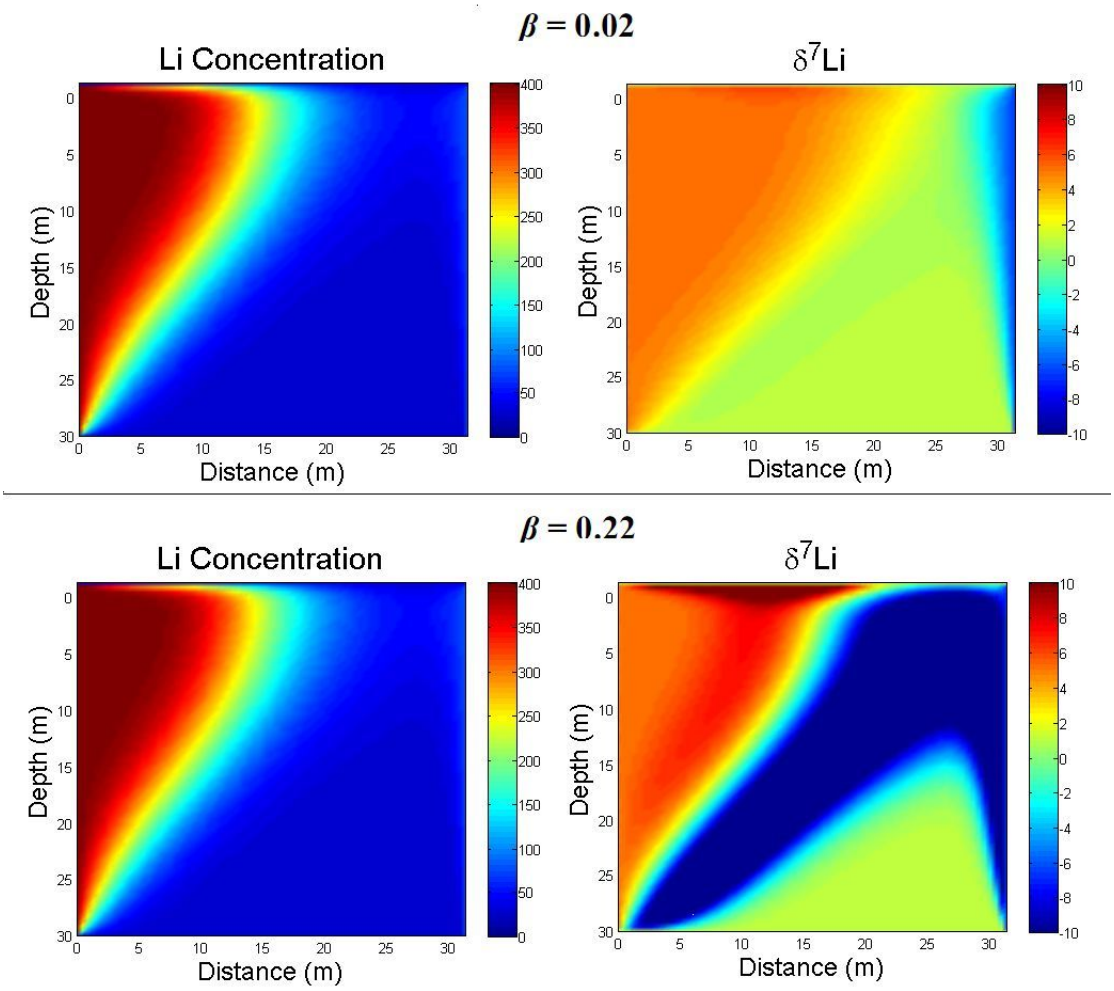

Figure 17. The influence of β on model outcomes for [Li] (left panels) and δ^7Li (right panels) distribution. In all models, *Pe*=5, C_L=400 ppm, and δ^7Li=+5.

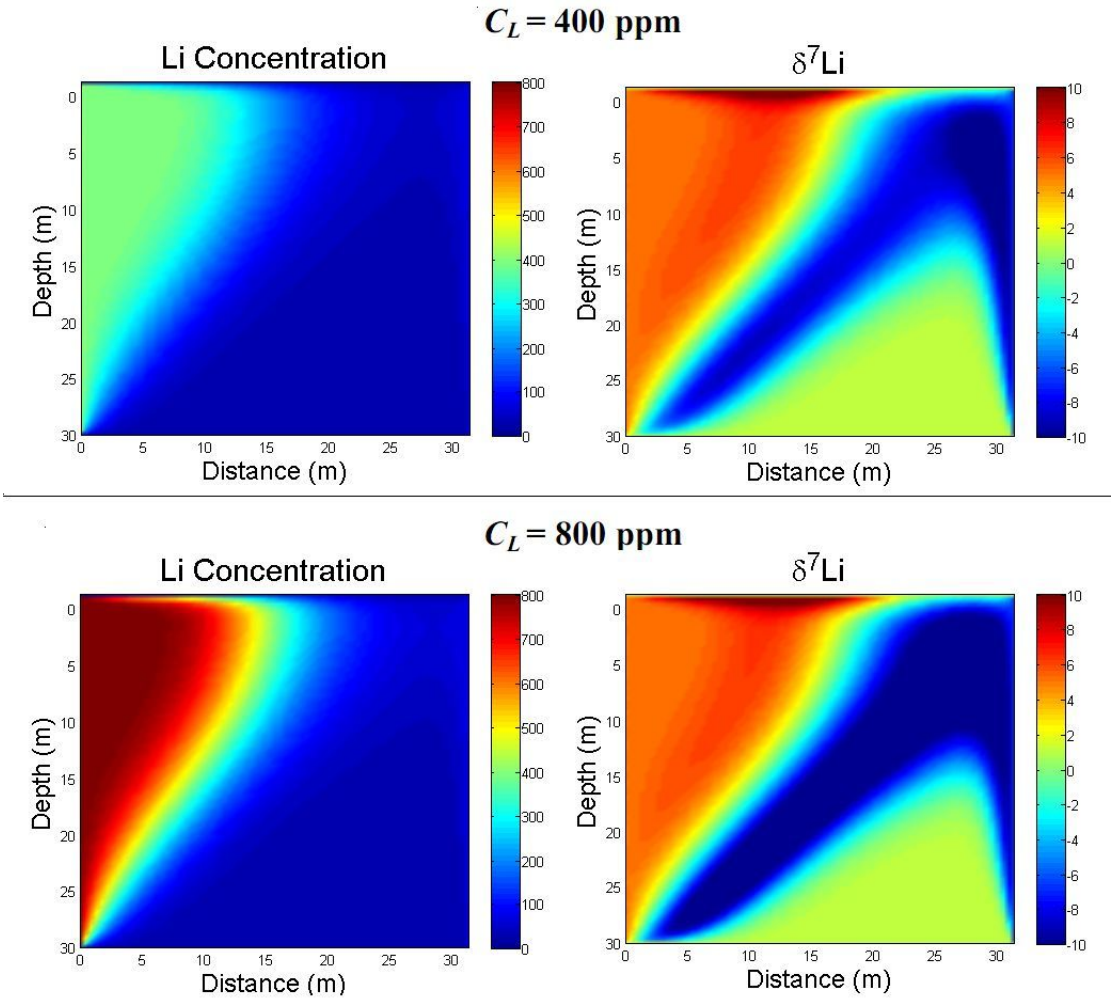

Figure 18. The influence of [Li] boundary conditions on model outcomes for [Li] (left panels) and δ^7Li (right panels) distribution. In all models, β=0.12, *Pe*=5, and δ^7Li=+5.

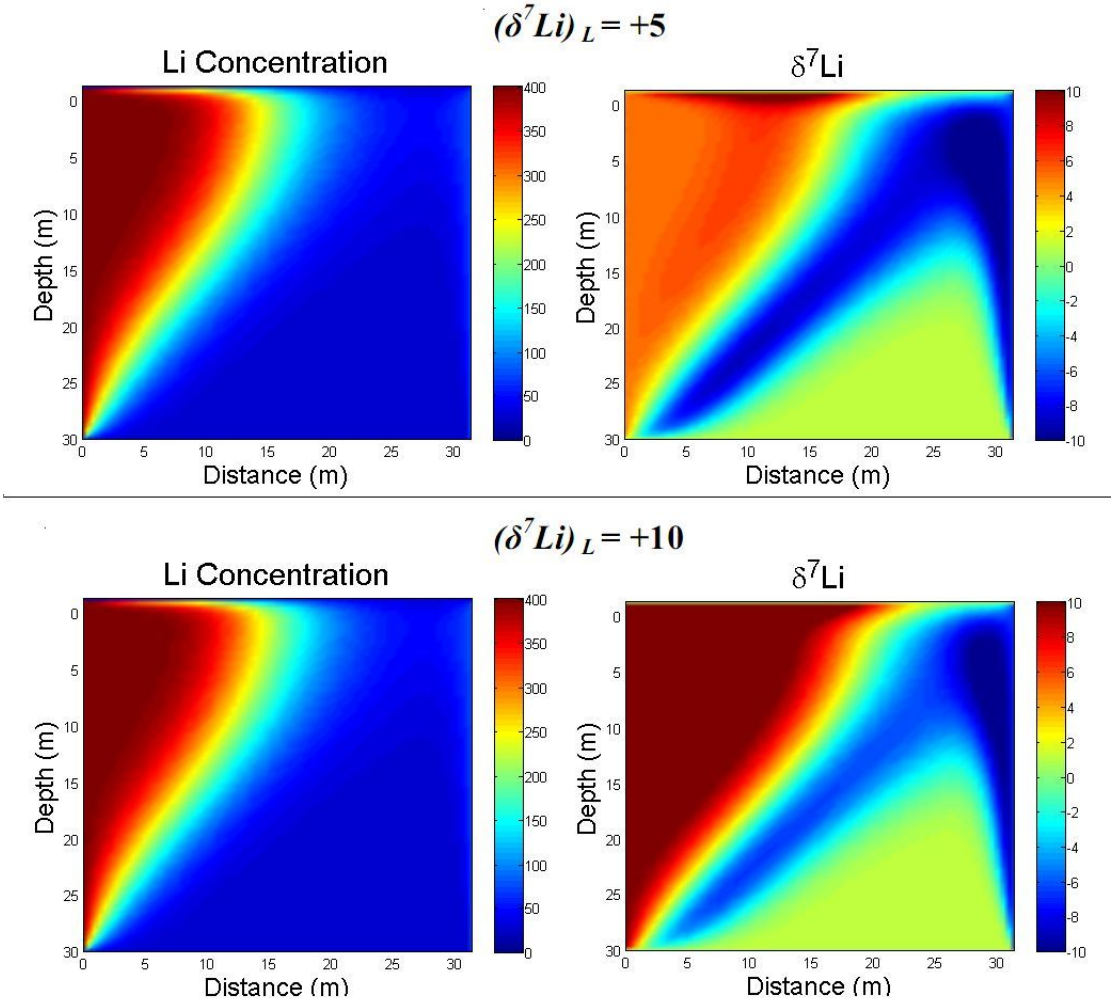

Figure 19. The influence of δ^7Li boundary conditions on model outcomes for [Li] (left panels) and δ^7Li (right panels) distribution. In all models, β=0.12, *Pe*=5, and C_L=400 ppm.

In sum, parameters that control the process of fluid percolation, such as the Peclet number, play an important role in controlling Li isotopic distribution in contact aureoles. β influences δ^7Li distributions but not Li concentration distributions. By contrast, parameters that define the boundary conditions, such as Li concentrations and δ^7Li values, do not have much influence on the Li concentration and δ^7Li distributions when allowed to vary within reasonable bounds.

Chapter 7: Discussion

In this chapter, the results from Li analyses and 2-D advection-diffusion modeling are combined in order to elucidate the mechanisms that control Li distribution in contact aureoles. Li elemental and isotopic behavior of fluids, as reflected by fluid inclusions and mineral separates from pegmatites, will be discussed in Section 7.1. Possible mechanisms of Li transport in the country rocks of the Florence County pegmatites are discussed in Section 7.2 and the Li concentration and δ^7Li distributions in the KX and ARA profiles are discussed in detail in Section 7.3.

7.1 Fluid Inclusions and Mineral Separates from Pegmatites

Isotopic compositions of Li in three fluid inclusion leachates of the KX pegmatite are uniformly heavy (δ^7Li= +18.0 to +19.9), which is consistent with the theory that ^{7}Li preferentially partitions into fluids during the fluid-rock (mineral) interactions (Teng et al., 2004). By contrast, δ^7Li values in mineral separates are heterogeneous, but consistently lighter, ranging from +1.5 in the KX spodumene to +8.2 in one of the ARA tourmalines (Table 4). The possible reasons for these very different δ^7Li signatures are explored below.

The presence of large variation of δ^7Li within single mineral types (e.g., Li-rich micas) illustrates the heterogeneity of the ARA pegmatites (Table 4). This heterogeneity may reflect different fluid-mineral partition coefficients, and/or kinetic fractionation associated with the very rapid crystallization of these pegmatite dikes (Sirbescu et al., 2008). For example, the equilibrium partition coefficients of Li isotopes between quartz and fluid appear to be different from that between mica and the same fluid, with quartz taking in ^{7}Li preferentially (e.g., Teng et al., 2006b).

However, this cannot explain the variations in δ^7Li in the same type of minerals. In these cases, the mineral-fluid interactions may not reach equilibrium, resulting in different mineral grains with various Li composition.

We use the experimental results of Wunder et al. (2007) to investigate whether the differences in δ^7Li between minerals and fluid results from equilibrium fractionation. The fractionation between mica and fluid is approximated by the following equation: $\Delta^7 Li_{mica-fluid} = -4.52 \times (1000/\mathrm{T(K)}) + 4.74$. Using the estimated temperature of the country rocks of the ARA profile of ~ 220°C (Sirbescu et al., 2008), $\Delta^7 Li_{mica-fluid}$ is calculated to be only -4.4, indicating Li-mica should have δ^7Li = +14.6 assuming δ^7Li of the fluid is +19. However, the δ^7Li values of the ARA micas vary from +2.0 to +8.0, suggesting that equilibrium fractionation is not the only mechanism producing Li isotopic fractionation between Li-micas and fluids.

We do not know the δ^7Li of the fluid associated with the KX pegmatite since all three fluid inclusions are from the ARA pegmatites. Using the spodumene data from the KX pegmatite and $\Delta^7 Li_{spondumene-fluid} = -4.61 \times (1000/\mathrm{T(K)}) + 2.48$ (Wunder et al., 2006), $\Delta^7 Li_{spod-fluid}$ is calculated to be -6.9 at ~220°C, corresponding to δ^7Li of ~+12 for the fluid. This value is similar to that measured from the fluid from the Tin Mountain pegmatite (Teng et al., 2006b).

The broad range of Li isotopic ratios in the pegmatitic minerals may be produced by kinetic rather than equilibrium fractionation. The variable Li concentrations and δ^7Li in mineral separates (spodumene, Li-rich mica and tourmaline) might be expected within a pegmatite since both fractional crystallization and kinetic effects can change the Li concentration and the isotopic composition from the margin of the pegmatite towards its core.

7.2 Controls on Li in Country Rock Profiles

While dehydration reactions may influence the Li distribution in country rocks of the contact aureoles, no evidence of dehydration from either the field or thin-sections was found. Furthermore, the study from Teng et al. (2007) concludes that metamorphic dehydration plays a minor role in Li isotopic composition of metapelitic country rocks. Thus, dehydration is unlikely to control Li distribution in the KX or ARA profiles.

The marked enrichment of Li in the country rocks in both the KX and ARA profiles relative to regional samples detailed in Chapter 4 is evidence that the Li-rich pegmatite intrusions increased the Li concentrations in their adjacent country rocks. Moreover, the decrease in δ^7Li with increasing distance away from both the KX and ARA pegmatite contacts is consistent with kinetic isotope fractionation produced as Li diffused from the pegmatites into the country rocks. Similar observations for the country rocks of the Tin Mountain pegmatite led Teng et al. to suggest Li diffusion through a grain-boundary fluid.

Two lines of evidence suggest an important role of fluids in transporting Li from the Wisconsin pegmatites to the country rocks. First, Li concentrations of amphiboles in amphibolite country rocks show a prominent decreasing trend with distance away from the KX contact on the tens of meters scale (Figure 7), indicating their equilibration with Li-carrying grain boundary fluids derived from the pegmatite. Second, the KX country rocks contain alteration minerals, such as chlorite, especially within the first few meters away from the main pegmatites contacts (Table A1 and Figure 6). This also suggests that the infiltration of fluids from the pegmatites into the country rocks occurred during pegmatite intrusion.

Below, the geochemical and modeling results are discussed for both the KX and ARA profiles. It is shown that diffusion alone cannot explain the observed lithium isotopic distribution, nor can a 2-D advection-diffusion process. Lithological heterogeneities and associated permeability variations are likely to have influenced the Li isotopic distribution along the two contact aureoles. Thus, the numerical modeling does not exactly match the geochemical observations, but rather, offers some insights on the physical processes and the most important parameters controlling Li distribution in metamorphic contact aureole settings.

7.2.1 King-X Road Cut Profile

As displayed in Figures 7 and 8, the Li concentration of amphiboles and whole rock δ^7Li distributions show decreasing trends with distance away from the KX contact. The distribution of Li isotopes may be explained by diffusion only or by combined diffusion-advection through grain boundary fluids. To quantify the effect of the magnitude of diffusion versus advection, the Peclet number, defined previously as $Pe = \frac{V_o L}{D_o}$, is used. That is to say, Pe goes to infinity if there is no diffusion and Pe is equal to zero if there is only diffusion and no advection. Each of these possibilities is described, in turn.

A 1-D diffusion model (Pe=0) has been used to explain Li elemental and isotopic distributions in contact aureoles from previous case studies, such as those in Teng et al. (2006a) and Marks et al. (2007). Here, I calculate a 1-D diffusion profile using the curve fitting tool of Matlab® to find the characteristic length of diffusion that best fits the geochemical observations for the KX profile. A characteristic length ($2\sqrt{Dt}$) of ~ 34 m and a β value of 0.06 are found to best fit the profile data (details are attached in Appendix C.). This best fit 1-D diffusion model is shown in Figure 20.

While it can explain the Li concentration distribution, it does not match the irregular distribution of δ^7Li through the country rocks. This suggests that Li isotopic distributions in the KX country rocks are likely to be controlled by an advection -diffusion process.

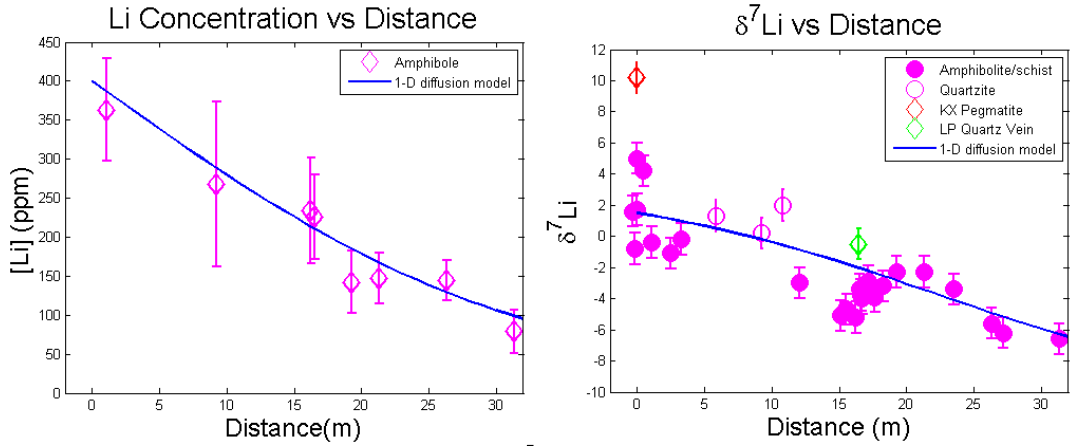

Figure 20. 1-D Diffusion model of [Li] and δ^7Li vs. distance plots for the KX Road Cut. Characteristic length is ~34 m and *Pe*=0 for diffusion only. δ^7Li of the pegmatite is assumed to be the same as for spodumene.

The 2-D advection-diffusion model for the KX profile is displayed in Figure 21. 2-D Li concentration and δ^7Li distributions are shown in colored maps on the left panel. To compare the δ^7Li distributions from numerical modeling with geochemical observation, 2-D Li concentration and δ^7Li distributions need to be converted to 1-D distributions, as every horizontal line on the 2-D distributions is a 1-D δ^7Li profile. To reflect the vertical variation of distribution, 1-D δ^7Li distributions are shown at three different depths (9, 16, and 22 m), which encompasses the mid-depth of the modeling domain and thus avoids the boundary effects in the upper left and lower right portions of the domain. In reality, the sampling transverse lines may not be exactly perpendicular to the contact and the contact may not be flat, which may account for some irregularities in the geochemical data. The model can explain the general behavior of Li isotopic fractionation along the contact, although it does not match the

geochemical data exactly, especially close to the contact. Moreover, the 1-D diffusion model seems to have done a better job explaining Li concentration distribution of the KX profile compared to the 2-D advection-diffusion model.

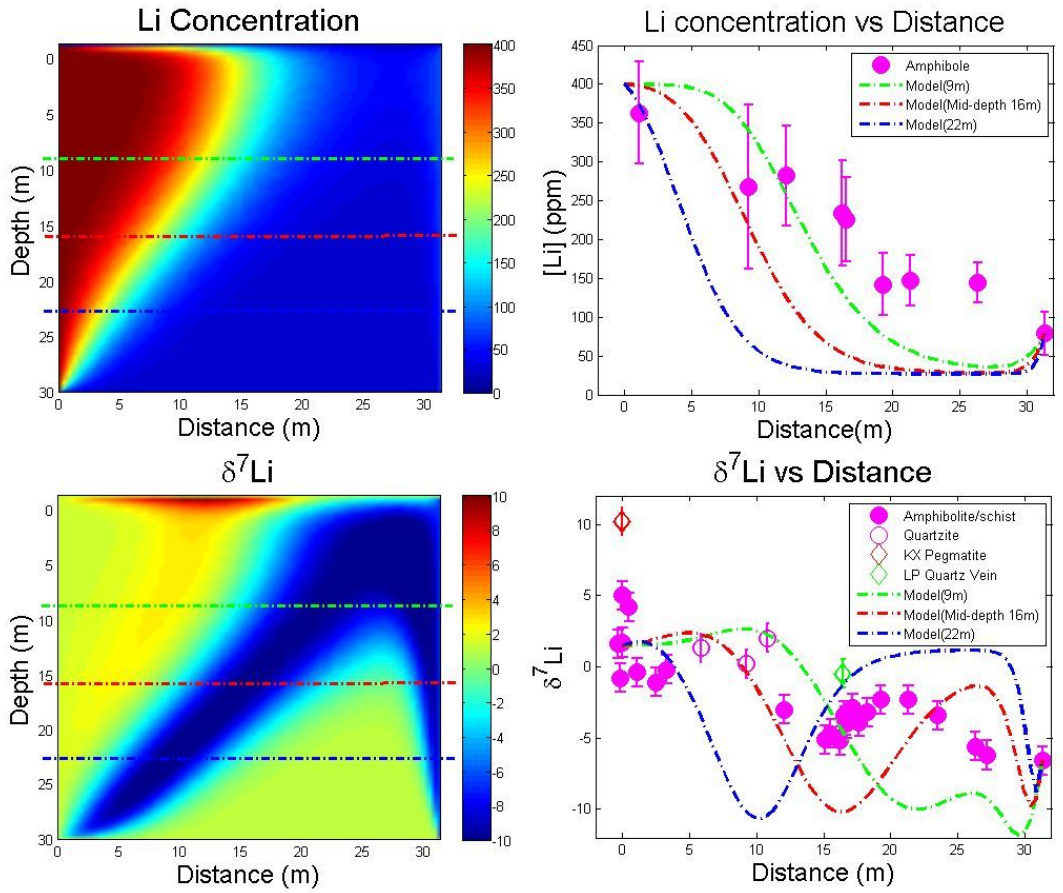

Figure 21. Combination of numerical solutions and geochemical observation on [Li] and δ^7Li vs. distance plots for the KX road cut. Left diagrams show 2-D [Li] (in ppm) and δ^7Li (in ‰) distributions and right diagrams display their corresponding 1-D distributions at different depths (9, 16, and 22 m) plotted with geochemical data. Boundary conditions for [Li] are 400 ppm for the left contact and 79 ppm at the right; δ^7Li is +1.5 for the left contact and -6.6 at the right.

In sum, neither 1-D diffusion nor 2-D advection-diffusion with constant permeability explains the geochemical observations of Li elemental and isotopic distributions well. Nevertheless, country rocks adjacent to the KX pegmatite are lithologically heterogeneous, as shown from both field and thin-sections. The irregularities of the lithium isotopic distribution in the KX profile are, thus, likely to

be a result of heterogeneous fluid flow caused by heterogeneous permeability in the country rocks, which implies that fluid advection occurred.

7.2.2 Animikie Red Ace Profile

Like the KX profile, Li concentration distributions in the country rocks of the ARA profile decrease, but do not show simple trends with distance away from the two bordering pegmatites. Also, like the KX profile, amphibolite and schist country rocks adjacent to the ARA pegmatites have much higher Li concentrations relative to their regional counterparts. Both the large Li concentration difference between country rocks and regional samples and the δ^7Li distribution indicate that the left ARA pegmatite (P1) has largely influenced the Li distribution in its country rocks. By contrast, the influence of the smaller ARA pegmatite on the right appears to be small.

The model for the ARA profile is plotted in Figure 22. The 2-D Li concentration and δ^7Li distributions are shown on the left panel. As for the KX profile, 1-D Li concentration and δ^7Li distributions are illustrated at three different depths (15, 30 and 45 m), which encompass the mid-depth of the modeling domain in order to avoid the effects at the boundaries. In addition, uncertainties regarding the true geometry of the sample profile (the degree of permeability and the straightness of the contact) may influence the comparisons. At any single depth, the model does not match the distribution of Li isotopic composition along the contact well, especially for the regions close to the ARA pegmatite intrusions. As shown from field geometry (see Figure 5), the country rock foliations are perpendicular to the exposure/modeling plane. Thus, the mismatches between the model and geochemical observations may be explained by heterogeneous permeability induced by this foliation structure within country rocks, if advection of fluids occurred. Therefore, diffusion is not likely to be the only mechanism that controls Li distributions in the ARA country rocks.

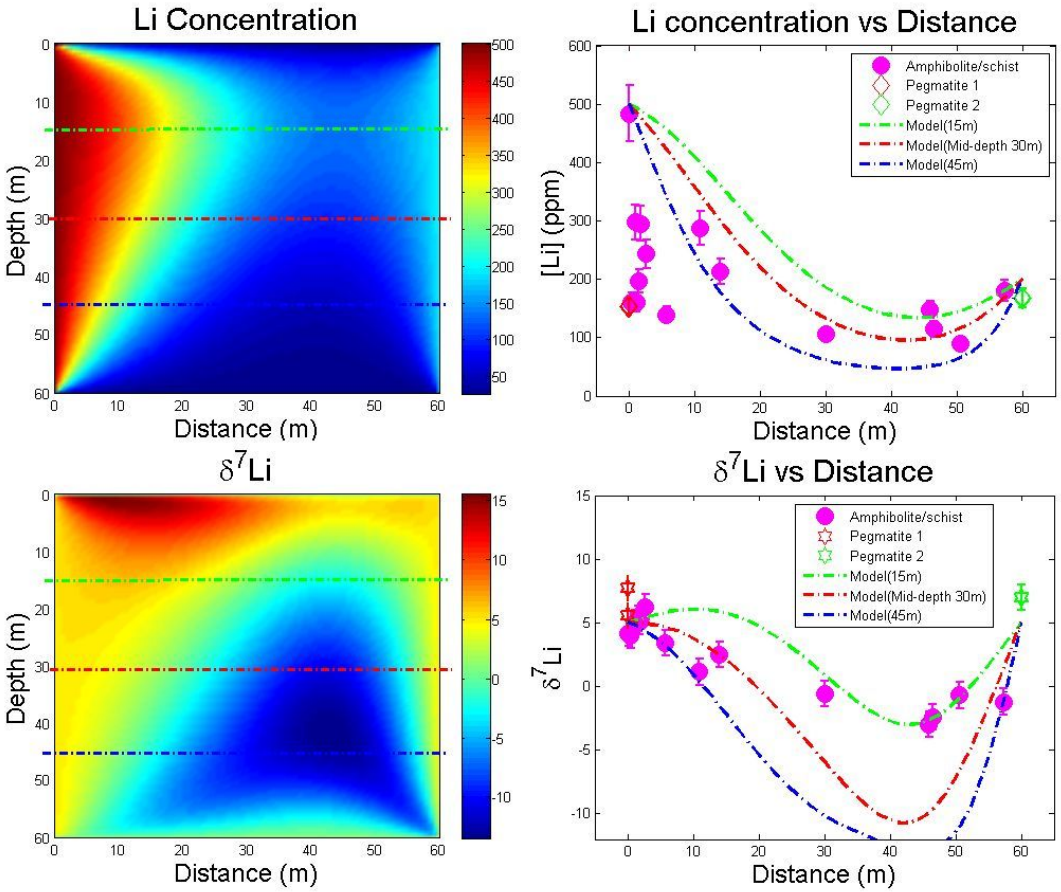

Figure 22. Combination of numerical solutions and geochemical observation on [Li] and δ^7Li vs. distance plots for the ARA profile. Left diagrams show 2-D [Li] (in ppm) and δ^7Li (in ‰) distributions and right diagrams display their corresponding 1-D distributions at different depths (15, 30, and 45 m) plotted with geochemical data. Boundary conditions for [Li] are 500 ppm for the left contact and 200 ppm at the right; δ^7Li is +5.0 for the left contact and -1.0 at the right.

Chapter 8: Conclusions

The pegmatite dikes in Florence County, Wisconsin, have had a large impact on the Li budget of their adjacent country rocks, with Li enriched up to a factor of twenty over regional values. Furthermore, Li from the pegmatite has travelled more than 50 meters into the country rocks. Simple diffusion of Li isotopes in a grain-boundary fluid cannot explain the Li isotopic distribution in country rocks, nor can 2-D advection-diffusion models. Rather, both fluid infiltration and diffusion from the pegmatites into heterogeneous country rocks are likely responsible for the increasing lithium content and isotopic distribution in country rocks of the Florence Country pegmatites. Permeability structure induced by lithological variation and/or foliation may also influence the heterogeneous distribution of Li isotopes in country rocks.

Peclet number plays an important role in determining both Li elemental and isotopic distributions within the country rocks adjacent to pegmatites, while β is important in determining Li isotopic distributions. By contrast, the Li concentration and isotopic composition of pegmatites have a minor influence in determining Li isotopes distributions in country rocks. Lithium isotopes are clearly sensitive tracers of fluid-rock interactions in country rocks adjacent to the pegmatites, at least on the tens of meters scale.

Appendices

A. Discretization of Governing Equations

A.1 Discretization for equation (7): $\nabla \cdot (\underline{\underline{\mathbf{K}}}^{-1} \nabla P) = 0$

$$a_p P_p = a_E P_E + a_W P_W + a_N P_N + a_S P_S$$

$$a_p = a_E + a_W + a_N + a_S$$

$$a_E = \frac{k_e \Delta y}{(\delta x)_e}$$

$$a_W = \frac{k_w \Delta y}{(\delta x)_w}$$

$$a_N = \frac{k_n \Delta x}{(\delta y)_n}$$

$$a_S = \frac{k_s \Delta x}{(\delta y)_s}$$

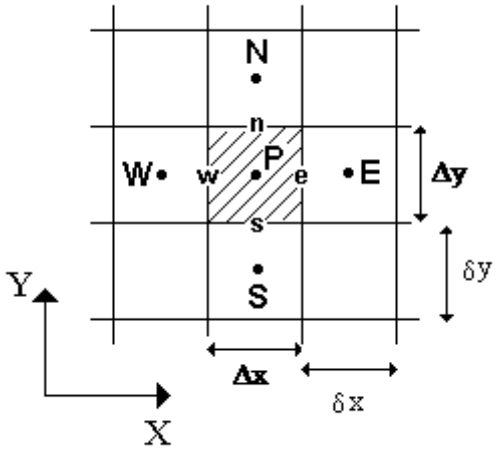

A.2 Discretization for equation (9): $\frac{\partial C}{\partial t} + \nabla \cdot (C \underset{\sim}{V}_f) = D \nabla^2 C$

$a_p C_p = a_E C_E + a_W C_W + a_N C_N + a_S C_S$, where

$a_p = a_E + a_W + a_N + a_S$,

$a_E = D_e A(|F_e|) + [[-F_e, 0]]$,

$a_W = D_w A(|F_w|) + [[F_w, 0]]$,

$a_N = D_n A(|F_n|) + [[-F_n, 0]]$,

$a_S = D_s A(|F_s|) + [[F_s, 0]]$;

where D_x is diffusion coefficient (take D_x=1)

$$F_e = u_e dy,$$
$$F_w = u_w dy,$$
$$F_n = v_n dx,$$
$$F_s = v_s dx.$$

According to Patankar (1980), F_x is formulated as follows:

$$A(|F_e|) = [[0, (1 - 0.1|F_e|)^5]],$$
$$A(|F_w|) = [[0, (1 - 0.1|F_w|)^5]],$$
$$A(|F_n|) = [[0, (1 - 0.1|F_n|)^5]],$$
$$A(|F_s|) = [[0, (1 - 0.1|F_s|)^5]].$$

B. Matlab® Codes

B.1 Main

```
clear all
% Define grid
dh=1/50;
dx=1/50;
dy=1/50;

% Set peclet number
Per=1;
% Calculate from pegmatite and regional samples
% Input
std=12.11;
Cintru=500;
dintru=10.2;
Cregion=27;
dregion=1.2;
% Calculate 7Li and 6Li conc
C6intru=Cintru/(1+std*(1+dintru/1000));
C7intru=Cintru-C6intru;
C6region=Cregion/(1+std*(1+dregion/1000));
C7region=Cregion-C6region;
% Set beta value
beta=0.15;
diffr=(7/6)^beta;
% Obtaining pressure, velocity, concentration and delta distributions
pressurevaryKKX
velocityvaryKKX
li7conc2KX
li6conc2KX
plotKX
```

B.2 Pressure solver

```
% Pressure solver for varying permeability(div [k[grid(P)]]=0) %
% by Xiaoming Liu %
% Modified on Jun 3, 2008 %
```

set up variables

```
J=1/dh+1;
L=1/dh+1;
% dh=1/(J-1);
% J=1/dh+1;
% L=1/dh+1;
% left boundary counts
rows=[J+1:J:L*(J-1)];
% right boundary counts
rows2=rows+J-1;
% total number of rows and columns in assembled matrix
i=J*L;

set up permeability matrix
% 1. random permeability %
K=rand(J,L);
```

```
% 2. Constant permeability %
K=ones(J,L);

% 3. vertical layered permeability %
% Mt=0.1;
% K=Mt*ones(J,L);
% k=2:2:L;
% K(:,k)=1;
```

set up A matrix roughly

```
A=zeros(L*J,L*J);
for j=2:1:J-1;
   for l=2:1:L-1;
   %East
   A((j-1)*L+l,(j-1)*L+l+1)=-(K(j,l+1)+K(j,l))/2;
   %West
   A((j-1)*L+l,(j-1)*L+l-1)=-(K(j,l-1)+K(j,l))/2;
   %North
   A((j-1)*L+l,j*L+l)=-(K(j+1,l)+K(j,l))/2;
   %South
   A((j-1)*L+l,(j-2)*L+l)=-(K(j-1,l)+K(j,l))/2;
   %Center
   A((j-1)*L+l,(j-1)*L+l)=(K(l,j+1)+K(l,j-1)+K(l+1,j)+K(l-1,j))/2+2*K(l,j);
   end
end

% set up A for up and bottom boudaries
A(1:L,:)=0; %bottom (side)%
A(J*(L-1)+1:L*J,:)=0; %top (side)%
A(1:L,1:J)=eye(L,J); %bottom (diagonal)%
A(J*(L-1)+1:L*J,L*(J-1)+1:L*J)=eye(J,L); %top (diagonal)%

% set up A for left and right boudaries
A(rows,:)=0; %left (side)%
A(rows2,:)=0; %right (side)%
for ii=1:size(rows,2);
A(rows(ii),rows(ii))=1; %left (diagonal)%
end;
for ii=1:size(rows2,2);
A(rows2(ii),rows2(ii))=1; %right (diagonal)%
end;
```

% Boundary Conditions (Can be changed as needed)

```
ii=1:i;
j=[1:1:J];
l=[1:1:L];
f(ii)=0;

% f((J-1)*L+l)=0.9;    %top%
f(l)=1.5;           %bottom%
f((j-1)*L+1)=1-(l-1)*dh+0.5;  %left%
f((j-1)*L+J)=1-(l-1)*dh;  %right%
```

solve for pressure P

```
P=A\(f');
```

convert result to 2-D matrix

```
for m=1:J
   for n=1:L
ii=(m-1)*L+n;
Pm(m,n)=P(ii);
   end
end
```

Plot

```
figure
x=[0:dh:1];
y=[0:dh:1];
pcolor(y,x,Pm);
shading('interp');
title('Pressure','FontSize', 18);
```

```
xlabel('Distance x','FontSize', 18);
ylabel('Depth y','FontSize', 18);
colorbar;
```

B.3 Velocity solver

```
% Velocity field solver for varying permeability %
% by Xiaoming Liu %
% Modified on Jun 3, 2008 %


%initial set up
gridx=1/dh+1;
gridy=1/dh+1;

% Initial settings
u=zeros(J,L);
v=zeros(J,L);

for j=2:gridx-1;
  for l=2:gridy-1;
%constant permeability
 v(j,l)=-K(j,l)*(Pm(j+1,l)-Pm(j-1,l))/(2*dh);
 u(j,l)=-K(j,l)*(Pm(j,l+1)-Pm(j,l-1))/(2*dh);
  end
end


%boundary settings
u(1,:)=u(2,:);
u(L,:)=u(L-1,:);
u(:,1)=u(:,2);
u(:,L)=u(:,L-1);
v(:,1)=v(:,2);
v(:,L)=v(:,L-1);
v(1,:)=v(2,:);
v(L,:)=v(L-1,:);


%plot
figure
x=[0:dh:1-dh];
y=[0:dh:1-dh];
quiver(x(1:8:1/dh),y(1:8:1/dh),u(1:8:1/dh,1:8:1/dh),v(1:8:1/dh,1:8:1/dh))
legend('velocity vector');
title('Velocity Distribution','FontSize', 18);
xlabel('Distance','FontSize', 18);
ylabel('Depth','FontSize', 18);
```

B.4 Concentration solvers

```
% Li Concentration solver (with advection effect) %
% by Xiaoming Liu %
% Dec 7, 2008 %
```

setting up

```
J=1/dh+1;
L=1/dh+1;
j=[1:1:J];
l=[1:1:L];
rows=[J+1:J:L*(J-1)];
rows2=rows+J-1;
i=J*L;
```

setting up velocity

```
ue=u;
uw=u;
vn=v;
vs=v;

for j=2:J-1;
  for l=2:L-1;
ue(j,l)=0.5.*(u(j,l+1)+u(j,l));
uw(j,l)=0.5.*(u(j,l-1)+u(j,l));
vn(j,l)=0.5.*(v(j+1,l)+v(j,l));
vs(j,l)=0.5.*(v(j-1,l)+v(j,l));
  end
```

```
end

% F values calculation
Fe=ue*dy;
FW=uw*dy;
Fn=vn*dx;
Fs=vs*dx;

% Diffusion Coefficient
D=1;
De=D;
Dw=D;
Dn=D;
Ds=D;


for j=1:J;
  for l=1:L;
% F values
Fe(j,l)=Per*ue(j,l)*dy;
FW(j,l)=Per*uw(j,l)*dy;
Fn(j,l)=Per*vn(j,l)*dx;
Fs(j,l)=Per*vs(j,l)*dx;

% Ap values
Ape(j,l)=max(0,(1-0.1*abs(Fe(j,l)))^5);
Apw(j,l)=max(0,(1-0.1*abs(Fw(j,l)))^5);
Apn(j,l)=max(0,(1-0.1*abs(Fn(j,l)))^5);
Aps(j,l)=max(0,(1-0.1*abs(Fs(j,l)))^5);

% set up the coefficients
ae(j,l)=De*Ape(j,l)+Per*max(-Fe(j,l),0);
aw(j,l)=DW*Apw(j,l)+Per*max(0,Fw(j,l));
an(j,l)=De*Apn(j,l)+Per*max(-Fn(j,l),0);
as(j,l)=Ds*Aps(j,l)+Per*max(0,Fs(j,l));
  end
end
```

set up A matrix roughly

```
A=zeros(J*L,J*L);
for j=2:J-1;
   for l=2:L-1;
A((j-1)*L+l,(j-1)*L+l+1)=-ae(j,l);
A((j-1)*L+l,(j-1)*L+l-1)=-aw(j,l);
A((j-1)*L+l,(j-1)*L+l+L)=-an(j,l);
A((j-1)*L+l,(j-1)*L+l-L)=-as(j,l);
A((j-1)*L+l,(j-1)*L+l)=ae(j,l)+aw(j,l)+an(j,l)+as(j,l);
   end
end

% set up A for up and bottom boudaries
A(1:L,:)=0;
A(J*(L-1)+1:L*J,:)=0;
A(1:L,1:J)=eye(L,J);
A(J*(L-1)+1:L*J,L*(J-1)+1:L*J)=eye(J,L);

% set up A for left and right boudaries
A(rows,:)=0;
A(rows2,:)=0;
for ii=1:size(rows,2);
A(rows(ii),rows(ii))=1;
end;
for ii=1:size(rows2,2);
A(rows2(ii),rows2(ii))=1;
end;
```

Boundary Conditions

```
ii=1:i;
j=[1:1:J];
l=[1:1:L];
Ci(ii)=0;
Ci((j-1)*L+1)=C7intru/Cintru;  %left%
% Ci(j*L)=C7intru2/Cintru;  %right%
Ci(j*L)=C7region/Cintru;  %right%
Ci((J-1)*L+j)=C7region/Cintru;    %top%
Ci(j)=C7region/Cintru;   %bottom%
```

solve for Concentration

```
C=A\Ci';
```

convert result to 2-D matrix

```
for m=1:J
   for n=1:L
ii=(m-1)*L+n;
Cm72(m,n)=C(ii);
   end
end
```

B.5 Plots

```
% length scale of the advection and diffusion process (characteristic length)
L=32;
% Convert 2-D conc to 1-D (averaged)
x=L*[0:dh:1]';
Cc72=(mean(Cintru*Cm72))';
Cc62=(mean(Cintru*Cm62))';
Lic=Cc72+Cc62;
```

a. Plot concentration in 2-D

```
figure
pcolor(x,x,Cm62+Cm72);
shading('interp');
title('2-D Concentration Plot','FontSize',18);
xlabel('Distance x','FontSize', 18);
ylabel('Depth y','FontSize', 18);
colorbar;
```

b. Concentration ploting

```
figure
%Retreive distance data from excel file
dis=xlsread('E:\plots.xls','plots','E6:E30')
conc=xlsread('E:\plots.xls','plots','C6:C30')
dispeg=xlsread('E:\plots.xls','plots','E4')
concpeg=xlsread('E:\plots.xls','plots','C4')
dispeg2=xlsread('E:\plots.xls','plots','E5')
concpeg2=xlsread('E:\plots.xls','plots','C5')
E=0.1*conc;
Epeg=0.1*concpeg;
Epeg2=0.1*concpeg2;
errorbar(dis,conc,E,'md','markersize',12,'LineWidth',2)
hold on;
errorbar(dispeg,concpeg,Epeg,'rd','markersize',12,'LineWidth',2)
hold on;
errorbar(dispeg2,concpeg2,Epeg2,'gd','markersize',12,'LineWidth',2)
hold on;
plot(x,Lic,'LineWidth',2,'color','b');
title('Li Concentration vs Distance Plot','FontSize',18);
xlabel('Distance','FontSize', 18);
ylabel('Li Concentration','FontSize', 18);
axis([-5 35 0 1000]);
```

c. Plot delta 7Li in 2-D

```
figure
pcolor(x,x,((Cm72./Cm62)/std-1)*1000);
shading('interp');
title('2-D delta 7Li Plot','FontSize',18);
xlabel('Distance x','FontSize', 18);
ylabel('Depth y','FontSize', 18);
colorbar;
```

d. Delta 7Li ploting

```
figure
%Retreive distance data from excel file
delta=xlsread('E:\plots.xls','plots','D6:D30')
deltapeg=xlsread('E:\plots.xls','plots','D4')
deltapeg2=xlsread('E:\plots.xls','plots','D5')
E=ones(size(dis),1);
```

```
Epeg=ones(size(dispeg),1);
Epeg2=ones(size(dispeg2),1);
errorbar(dis,delta,E,'md','markersize',12,'LineWidth',2)
hold on;
errorbar(dispeg,deltapeg,Epeg,'rh','markersize',12,'LineWidth',2)
hold on;
errorbar(dispeg2,deltapeg,Epeg2,'gh','markersize',12,'LineWidth',2)
hold on;
mdelta=((Cc72./Cc62)/std-1)*1000;
hold on;
plot(x,mdelta,'LineWidth',2,'color','b');
title('delta 7Li vs Distance Plot','FontSize',18);
xlabel('Distance x','FontSize', 18);
ylabel('delta 7Li','FontSize', 18);
axis([-5 30 -10 12]);
```

C. Validation of Codes

C.1a Analytical solution of Laplace equation

$$\frac{\partial^2 P}{\partial x^2}+\frac{\partial^2 P}{\partial y^2}=0 \quad \text{or} \quad \Delta P=0$$

Boundary conditions:

P (0, y) = 0
P (1, y) = 0
P (x, 0) = 0
P (x, 1) = 1
Using separation of variables, to assume P (x, y) = X (x) Y (y):

$$X''Y + XY'' = 0$$

$$-\frac{X''}{X}=\frac{Y''}{Y}=\lambda^2 \quad \text{, where } \lambda \text{ is a constant.}$$

$$X''(x) = -\lambda^2 X(x)$$
$$Y''(y) = \lambda^2 Y(y)$$

Therefore,
$$X(x) = C_1\cos(\lambda x)+C_2\sin(\lambda x)$$
$$Y(y) = C_3 e^{\lambda y}+C_4 e^{-\lambda y}$$

$$P(x, y) = [\, C_1\cos(\lambda x)+C_2\sin(\lambda x)\,]\,[\, C_3 e^{\lambda y}+C_4 e^{-\lambda y}\,]$$

Substitute boundary conditions into the above equation,

We get $$P(x,y)=\sum_{n=1}^{\infty} 2\frac{1-(-1)^n}{n\pi(e^{n\pi}-e^{-n\pi})}\sin(n\pi x)(e^{n\pi y}-e^{-n\pi y})$$

C.1b Comparison of Pressure Laplace solver (numerical solution) and analytical solution

```
% TEST of 'Pressure solver for constant permeability' %
% 2-D laplace equation (solve Pxx+Pyy=0)%
% by Xiaoming Liu %
% Created on April 1, 2009 %
```

[1].NUMERICAL SOLUTION

Set up variables

```
dx=1/50;
dy=1/50;
J=1/dx+1;
L=1/dy+1;
% left boundary counts
rows=[J+1:J:L*(J-1)];
% right boundary counts
rows2=rows+J-1;
% total number of rows and columns in assembled matrix
i=J*L;


% set up A matrix roughly
A0=4*ones(L*J,1);
A1=-1*ones(L*J-1,1);
A2=-1*ones((L-1)*J,1);
A=diag(A0)+diag(A1,1)+diag(A1,-1)+diag(A2,L)+diag(A2,-L);

% set up A for up and bottom boudaries
A(1:L,:)=0; %bottom (side)%
A(J*(L-1)+1:L*J,:)=0; %top (side)%
A(1:L,1:J)=eye(L,J); %bottom (diagonal)%
A(J*(L-1)+1:L*J,L*(J-1)+1:L*J)=eye(J,L); %top (diagonal)%

% set up A for left and right boudaries
A(rows,:)=0; %left (side)%
A(rows2,:)=0; %right (side)%
for ii=1:size(rows,2);
A(rows(ii),rows(ii))=1; %left (diagonal)%
end;
for ii=1:size(rows2,2);
A(rows2(ii),rows2(ii))=1; %right (diagonal)%
end;
```

Boundary Conditions (Can be changed as needed)

```
ii=1:i;
j=[1:1:J];
l=[1:1:L];
f(ii)=0;
f((j-1)*L+1)=0;  %left%
f((j-1)*L+J)=0;  %right%
% x=(l-1)*dx;
% y=(j-1)*dy;
f((J-1)*L+l)=1;  %top%
f(l)=0;   %bottom%
% solve for pressure P
P=A\(f');

% convert result to 2-D matrix
for m=1:J
    for n=1:L
ii=(m-1)*L+n;
Pm(m,n)=P(ii);
    end
end
```

[2].ANALYTICAL SOLUTION

```
for m=1:1:1/dx+1
    x=(m-1)*dx;
    if x==0
        Pa(n,m)=0;  %left boundary
    elseif x==1
        Pa(n,m)=0;  %right boundary
    end
    for n=1:1:1/dy+1
```

```
        y=(n-1)*dy;
        if y==0
            Pa(n,m)=0;   %bottom boundary
        elseif y==1
            Pa(n,m)=1;  %top boundary
        else
            Pa(n,m)=0;
            for N=1:2:101

Pa(n,m)=Pa(n,m)+4*sin(N*pi*x)*(exp(N*pi*y)exp(N*pi*y))/(N*pi*(exp(N*pi)-exp(-N*
pi)));
            end
        end
    end
end

% Plots
x=[0:dx:1];
y=[0:dy:1];

pcolor(y,x,Pa);
shading('interp');
title('Analytical Solution Pressure','FontSize', 18);
xlabel('Distance x','FontSize', 18);
ylabel('Depth y','FontSize', 18);
colorbar;
figure

pcolor(y,x,Pm);
shading('interp');
title('Numerical Solution Pressure','FontSize', 18);
xlabel('Distance x','FontSize', 18);
ylabel('Depth y','FontSize', 18);
colorbar;
figure

pcolor(y,x,Pa-Pm);
shading('interp');
title('Pa-Pm','FontSize', 18);
xlabel('Distance x','FontSize', 18);
ylabel('Depth y','FontSize', 18);
colorbar;
```

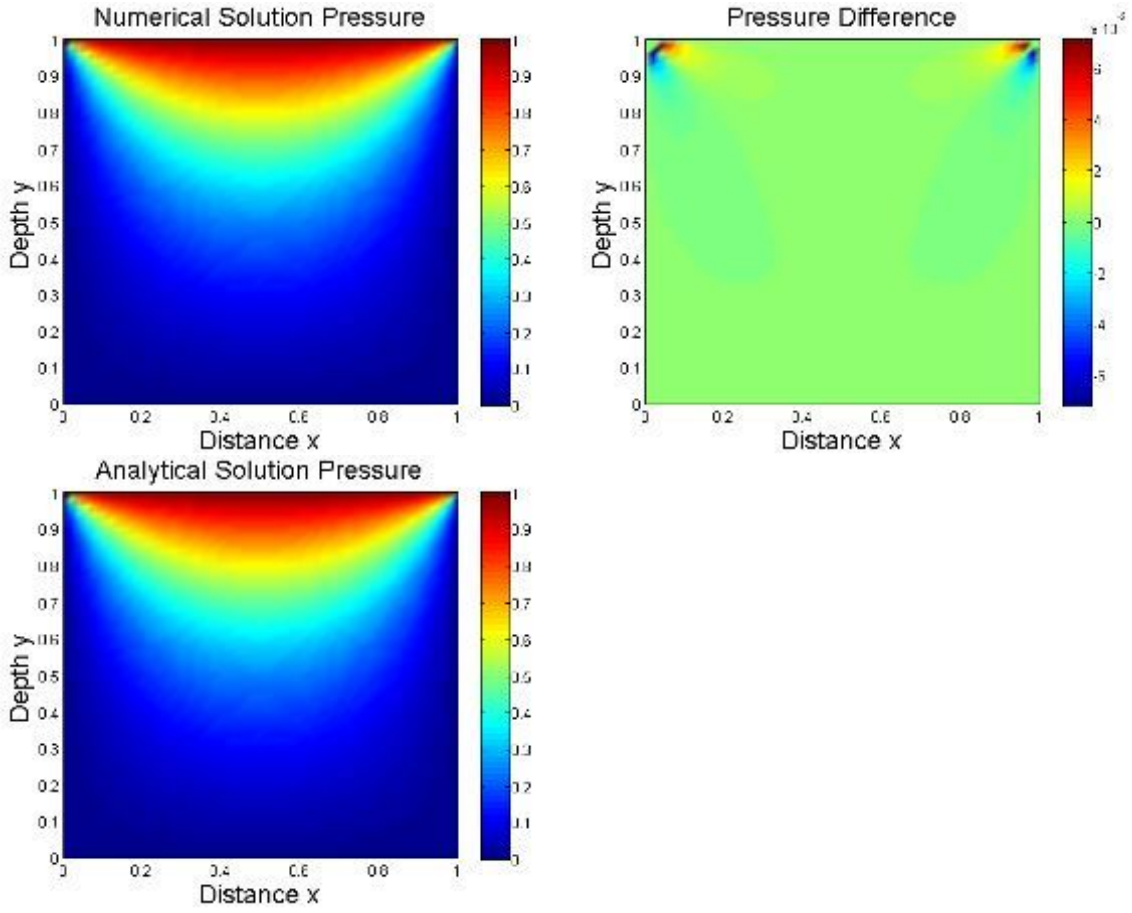

The analytical solution of pressure is

$P(x,y)=\sum_{n=1}^{\infty}2\frac{1-(-1)^n}{n\pi(e^{n\pi}-e^{-n\pi})}\sin(n\pi x)(e^{n\pi y}-e^{-n\pi y})$ as shown in A3.1. P does not change much when n is big enough. Thus, n=101 used to obtain the analytical solution is a good enough approximation.

Analytical solution and numerical solution are plotted as above. Also, the difference (error) between analytical solution and numerical solution is shown, where most of the error are approximately zero. The maximum error is less than ~1%. This proved the Laplace solver of the pressure is a good approximation of the analytical solution.

C.2a Analytical solution of advection-diffusion equation

$$\frac{\partial^2 C}{\partial x^2}+\frac{\partial^2 C}{\partial y^2}=\frac{\partial (V_x C)}{\partial x}+\frac{\partial (V_y C)}{\partial y} \quad \text{or} \quad \Delta C=\nabla\cdot(C\mathbf{V})$$

Take a simple case to do this validation of numerical solution where V_y=0 and V_x=1.

$$\frac{\partial^2 C}{\partial x^2}+\frac{\partial^2 C}{\partial y^2}=\frac{\partial C}{\partial x}$$

Boundary conditions:

C (0, y) = 0

C (1, y) = 1

C (x, 0) = 0

C (x, 1) = 0

Using separation of variables, to assume C (x, y) = X (x) Y (y):

$$\mathrm{X''Y+XY''=X'Y}$$

$$\frac{\mathrm{X'-X''}}{\mathrm{X}}=\frac{\mathrm{Y''}}{\mathrm{Y}}=-\lambda^2 \quad ,\lambda \text{ is a constant.}$$

$$\mathrm{X''(x)}-X'(x)-\lambda^2\,\mathrm{X(x)}=0$$

$$\mathrm{Y''(y)}+\lambda^2\,\mathrm{Y(y)}=0$$

Therefore, $\begin{aligned} X(x)&=C_1 e^{r1x}+C_2 e^{r2x} \\ Y(y)&=C_3\cos(\lambda y)+C_4\sin(\lambda y)\end{aligned}$,

where $r1=\dfrac{1+\sqrt{1+4\lambda^2}}{2}$ & $r2=\dfrac{1-\sqrt{1+4\lambda^2}}{2}$.

C (x, y) = $[\,C_1 e^{r1x}+C_2 e^{r2x}\,]\,[\,C_3\cos(\lambda y)+C_4\sin(\lambda y)\,]$

Substitute boundary conditions into the above equation,

We get $C(x,y)=\sum_{n=1}^{\infty} 2\dfrac{1-(-1)^n}{n\pi(e^{r1}-e^{r2})}\sin(n\pi y)(e^{r1x}-e^{r2x})$, where $r1=\dfrac{1+\sqrt{1+4\lambda^2}}{2}$

& $r2=\dfrac{1-\sqrt{1+4\lambda^2}}{2}$.

C.2b Comparison of advection-diffusion solver (numerical solution) and analytical solution

```
% TEST of 'Li diffusion-advection' %
% 2-D advection to diffusion(Pe=1, solve Cxx+Cyy=Cx) %
% by Xiaoming Liu %
% April 1, 2009 %
```

[1].NUMERICAL SOLUTION

```
dh=1/50;
dx=1/50;
dy=1/50;
% Set Peclet number
Per=1;
pressureconsKTEST
velocityconsKTEST
% setting up
J=1/dx+1;
L=1/dy+1;
j=[1:1:J];
l=[1:1:L];
rows=[J+1:J:L*(J-1)];
rows2=rows+J-1;
i=J*L;
```

Setting up velocity

```
ue=u;
uw=u;
vn=v;
vs=v;
for j=2:J-1;
  for l=2:L-1;
ue(j,l)=0.5.*(u(j,l+1)+u(j,l));
uw(j,l)=0.5.*(u(j,l-1)+u(j,l));
vn(j,l)=0.5.*(v(j+1,l)+v(j,l));
vs(j,l)=0.5.*(v(j-1,l)+v(j,l));
  end
end

% F values calculation
Fe=ue*dy;
Fw=uw*dy;
Fn=vn*dx;
Fs=vs*dx;

% Diffusion Coefficient
D=1;
De=D;
DW=D;
Dn=D;
Ds=D;

for j=1:J;
  for l=1:L;
% F values
Fe(j,l)=Per*ue(j,l)*dy;
Fw(j,l)=Per*uw(j,l)*dy;
Fn(j,l)=Per*vn(j,l)*dx;
Fs(j,l)=Per*vs(j,l)*dx;

% Constant Peclet numbers
pe(j,l)=Fe(j,l)/De;
pw(j,l)=Fw(j,l)/Dw;
pn(j,l)=Fn(j,l)/Dn;
ps(j,l)=Fs(j,l)/Ds;

% Ap values
Ape(j,l)=max(0,(1-0.1*abs(pe(j,l)))^5);
Apw(j,l)=max(0,(1-0.1*abs(pw(j,l)))^5);
Apn(j,l)=max(0,(1-0.1*abs(pn(j,l)))^5);
Aps(j,l)=max(0,(1-0.1*abs(ps(j,l)))^5);

% set up the coefficients
ae(j,l)=De*Ape(j,l)+Per*max(-Fe(j,l),0);
aw(j,l)=Dw*Apw(j,l)+Per*max(0,Fw(j,l));
an(j,l)=De*Apn(j,l)+Per*max(-Fn(j,l),0);
as(j,l)=Ds*Aps(j,l)+Per*max(0,Fs(j,l));
  end
end
```

Set up A matrix roughly

```
A=zeros(J*L,J*L);
for j=2:J-1;
   for l=2:L-1;
A((j-1)*L+l,(j-1)*L+l+1)=-ae(j,l);
A((j-1)*L+l,(j-1)*L+l-1)=-aw(j,l);
A((j-1)*L+l,(j-1)*L+l+L)=-an(j,l);
A((j-1)*L+l,(j-1)*L+l-L)=-as(j,l);
A((j-1)*L+l,(j-1)*L+l)=ae(j,l)+aw(j,l)+an(j,l)+as(j,l);
   end
end

% set up A for up and bottom boudaries
A(1:L,:)=0;
A(J*(L-1)+1:L*J,:)=0;
A(1:L,1:J)=eye(L,J);
A(J*(L-1)+1:L*J,L*(J-1)+1:L*J)=eye(J,L);

% set up A for left and right boudaries
A(rows,:)=0;
A(rows2,:)=0;
for ii=1:size(rows,2);
A(rows(ii),rows(ii))=1;
end;
for ii=1:size(rows2,2);
A(rows2(ii),rows2(ii))=1;
end;
```

Boundary Conditions

```
ii=1:i;
j=[1:1:J];
l=[1:1:L];
Ci(ii)=0;

Ci((J-1)*L+j)=0;    %top%
Ci(j)=0;    %bottom%
Ci((j-1)*L+1)=0;  %left%
Ci(j*L)=1;  %right%
% solve for Concentration
C=A\Ci';
```

Convert result to 2-D matrix and plot

```
for m=1:J
   for n=1:L
ii=(m-1)*L+n;
Cm(m,n)=C(ii);
   end
end
```

[2].ANALYTICAL SOLUTION

```
for m=1:1:1/dx+1
   x=(m-1)*dx;
   for n=1:1:1/dy+1
      y=(n-1)*dy;
      if y==0
         Ca(n,m)=0;   %bottom boundary
      elseif y==1
         Ca(n,m)=0;  %top boundary
      else
         Ca(n,m)=0;
         for N=1:2:101
            r1=(1+(1+4*(N*pi)^2)^0.5)/2;
            r2=(1-(1+4*(N*pi)^2)^0.5)/2;
 Ca(n,m)=Ca(n,m)+4*sin(N*pi*y)*(exp(r1*x)-exp(r2*x))/(N*pi*(exp(r1)-exp(r2)));
         end
      end
          if x==0
          Ca(n,m)=0;  %left boundary
          elseif x==1
          Ca(n,m)=1;  %right boundary
          end
   end
end

% Plots
x=[0:dx:1];
```

```
y=[0:dy:1];
pcolor(y,x,Ca);
shading('interp');
title('Analytical Solution Concentration','FontSize',18);
xlabel('Distance x','FontSize', 18);
ylabel('Depth y','FontSize', 18);
colorbar;
figure

pcolor(y,x,Cm);
shading('interp');
title('Numerical Solution Concentration','FontSize', 18);
xlabel('Distance x','FontSize', 18);
ylabel('Depth y','FontSize', 18);
colorbar;
figure
pcolor(y,x,Ca-Cm);
shading('interp');
title('Ca-Cm','FontSize', 18);
xlabel('Distance x','FontSize', 18);
ylabel('Depth y','FontSize', 18);
colorbar;
```

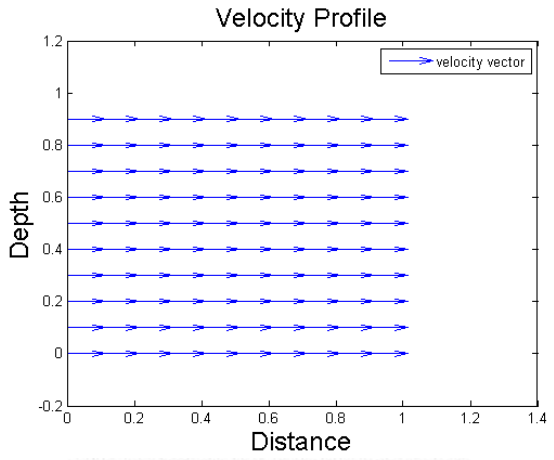

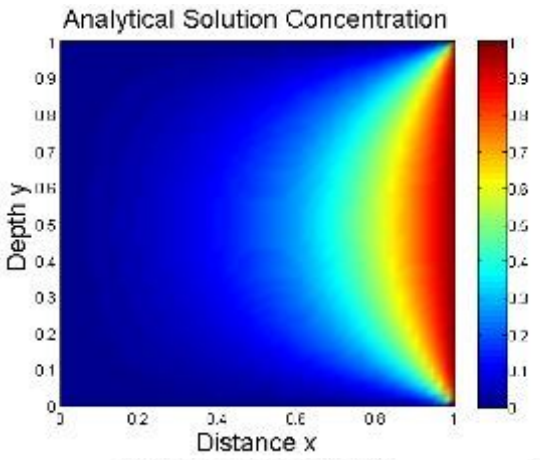

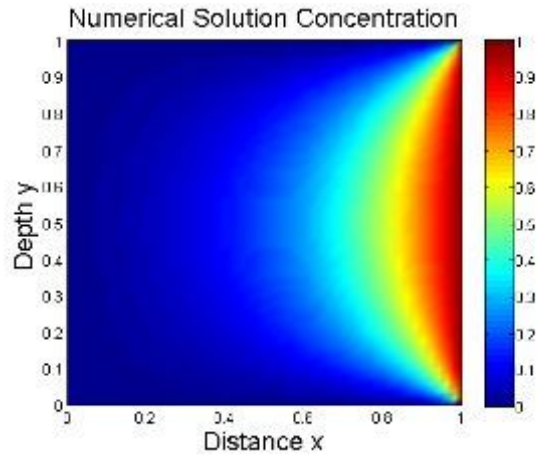

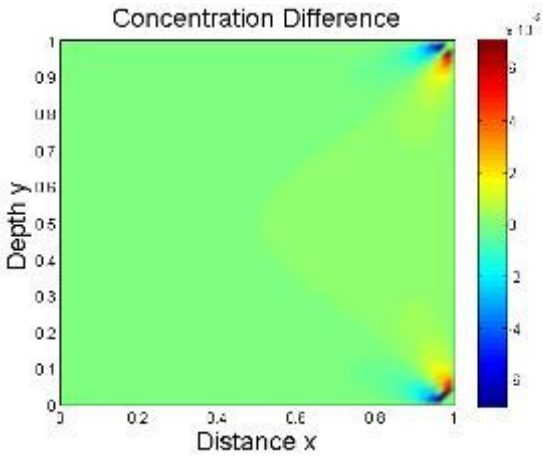

The analytical solution of advection-diffusion equation is

$$C(x,y)=\sum_{n=1}^{\infty}2\frac{1-(-1)^n}{n\pi(e^{r1}-e^{r2})}\sin(n\pi y)(e^{r1x}-e^{r2x}),\ \text{where}\ \ r1=\frac{1+\sqrt{1+4\lambda^2}}{2}\ \ \&$$

$$r2=\frac{1-\sqrt{1+4\lambda^2}}{2}.$$

This is shown in A3.2. C does not change much when n is big enough. So, n=101 used to obtain the analytical solution is a good enough approximation.

Analytical solution and numerical solution are plotted as above for concentration distribution. Also, error of numerical solution is shown, most of which are approximately zero. The maximum error is less than ~1%. This proved the advection-diffusion solver of the pressure is a good approximation of the analytical solution in the case of V_x=1 and V_y=0.

C.3 Comparison of analytical solution of 1-D diffusion equation with numerical solution

The equation of 1-D diffusion at the steady-state conditions is

$$\frac{\partial^2 C}{\partial x^2}=0$$

Boundary conditions:

C_o = 1 & C_1= 0

Therefore, the analytical solution can be obtained:

C=- $C_o x$+ C_o

The following codes were used to plot numerical and analytical solutions of 1-D diffusion (The numerical solution was obtained from modification of the 2-D concentration solvers).

```
x=[0:dh:1]';
CL=1;
l=[1:1:L];
Cc72=Cm72((L-1)/2,l)';
Cc62=Cm62((L-1)/2,l)';
Lic=Cc72+Cc62;
```

1-D analytical solution element conc and delta 7Li at the contact

```
Co=1;
do=10;
% element conc and delta 7Li in the regional rocks
C1=0;
d1=0;
% 7Li and 6Li calculations
Co6=Co/(1+std*(1+do/1000));
Co7=Co-Co6;
C16=C1/(1+std*(1+d1/1000));
C17=C1-C16;
% concentration calcuation for 7Li and 6Li
Cx7=-Co7*(x-1)/CL;
Cx6=-Co6*(x-1)/(CL*(diffr^0.5));

% Plot [Li] in 1-D
figure
plot(x,Cx7+Cx6,'LineWidth',2,'color','r','Linestyle','.');
hold on;
plot(x,Lic,'LineWidth',2,'color','b','Linestyle','-.');
% plot(x,Cx7+Cx6-Lic,'LineWidth',2,'color','g','Linestyle',':');
% plot(xn,Cx7+Cx6-Lic,'LineWidth',2,'color','g');
% title('Li Concentration vs Distance Plot','FontSize',18);
xlabel('Distance','FontSize', 18);
ylabel('Li Concentration','FontSize', 18);
axis([0 1 0 1]);
legend('Analytical solution','Numerical solution')


% Plot [Li] in 2-D
figure
pcolor(x,x,Cm62+Cm72);
shading('interp');
title('2D Concentration Plot-Numerical Solution','FontSize',18);
xlabel('Distance x','FontSize', 18);
ylabel('Depth y','FontSize', 18);
colorbar;
```

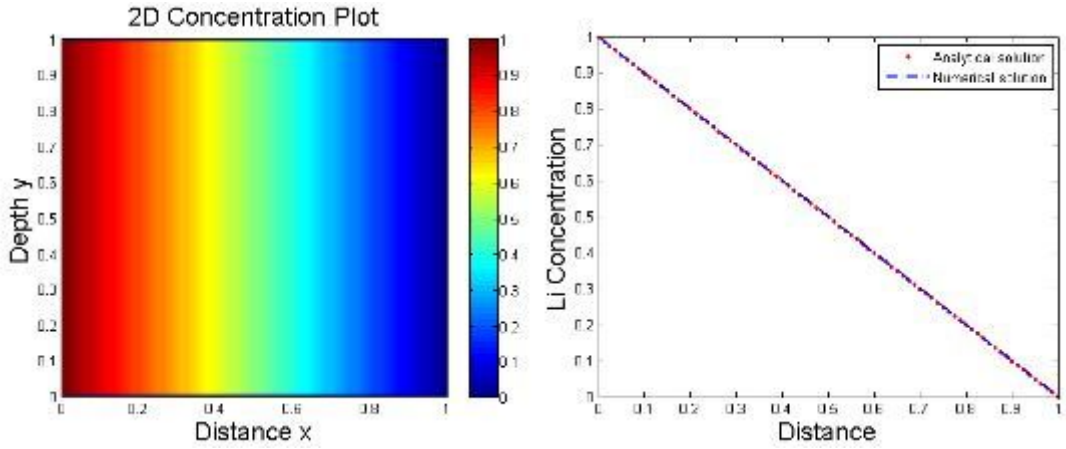

The left panel shows 2-D Li concentration distribution from numerical model. And the right panel shows the plots of both analytical and numerical solutions of the 1-D diffusion model. The nice match between these two solutions indicates the numerical model is good.

C.6 Characteristic length of 1-D diffusion model

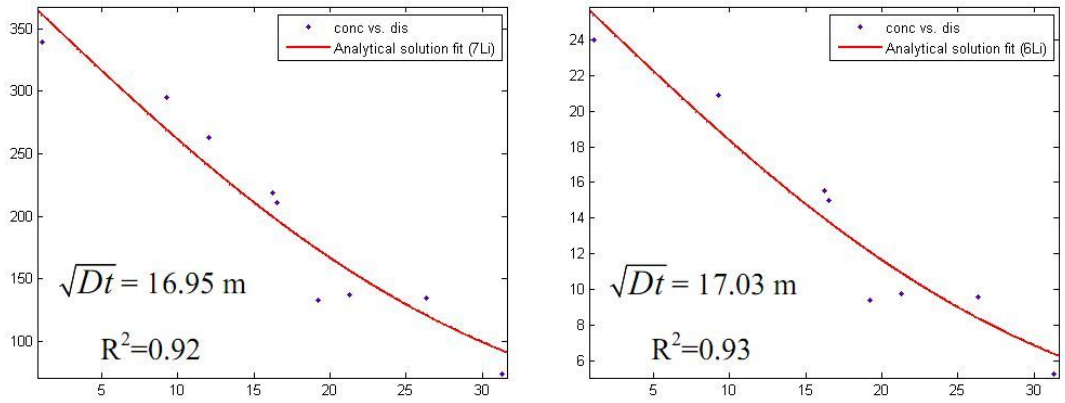

The best fit of amphibole Li concentration from the KX profile is calculated for both ^{7}Li and ^{6}Li. R^2 is the coefficient of determination, which ranges from 0 to 1. The value 1 indicates perfect fit. In both case, R^2 is better than 0.9, indicating good fits. The characteristic length of diffusion is $2\sqrt{Dt}$, which means the length is roughly 33.9 m and 34.0 m for 7Li and 6Li, respectively.

D. Appendix Tables

Table A 1. Petrography of samples.

Sample #	Sample Name	Major Minerals	Accessory Minerals	Notes
KX PROFILE				
LP1	Quartz vein	Am,Qtz,Fsp,Ms	Op	
LP2	Amphibolite	Am,Fsp,Qtz,Cb	Bt,Ttn	
LP6	Amphibolite	Am,Fsp,Qtz,Cb,Bt	Ttn	good foliation, Qtz grains are small, hard to distinguish Qtz and Fsp
LP8	Amphibolite	Am,Fsp,Qtz,Cb	Chl	
LP21	Amphibolite	Am,Cb,Fsp,Qtz,Pl	Ttn, Op	
LP26	Quartzite	Qtz, Am	Op,Cb	>90% Qtz
LP27	Quartzite	Qtz, Am,Cb	Op,Ttn,Chl,Bt	
LP30	Amphibolite	Am,Cb,Qtz	Ep	
LP31	Schist	Bt,Cb,Qtz	Op,Ttn,Chl,Bt	
LP32	Schist	Bt,Qtz	Cb,Ttn	
LP33b	Schist	Ep, Qtz,Fsp,Cb	Chl,Bt	Am altered to Ep
KX01	Pegmatite	Fsp,Qtz	Ms,Blue Am	
KX03	Schist	Fsp,Qtz,Cb,Ep	Am,Chl,Ky	
KX05	Schist	Qtz,Fsp,Am,Cb,Bt,Ep,Chl	Op	Am/Qtz cluster Bt/Chl/Ep aggregate

Table A1. Petrography of samples, continued.

Sample #	Sample Name	Major Minerals	Accessory Minerals	Notes
ARA PROFILE				
ARA1a	Pegmatite	Pl,Qtz,Tur	Blue Am/Tur?	Pl-rich
ARA1b	Pegmatite	Tur,Qtz,Ms		alteration, Tur-rich
ARA2a	Schist	Qtz,Bt,Fsp	Ep,Am,Ms	Fsp highly altered, cut parallel to foliation
ARA2h	Schist	Qtz,Fsp,Bt	Ms,Ep	Fsp altered to Ser
ARA2l	Schist	Qtz,Chl,Bt,Ep		aggregated Chl
ARA2O	Amphibolite	Am,Qtz,Ep	Op	Am highly altered
ARA2P	Amphibolite	Am,Qtz,Bt	Op	Am is fresh with good cleavages
08-P-06	Pegmatite	Pl,Qtz,Ep	Ms,Ser	
REGIONAL				
QFM1	Schist	Qtz,Fsp,Bt,Cb		
QFM3	Schist	Qtz,Fsp,Am,Bt	Op,Ep	Fsp altered to Ser, very heterogenous mineral distribution
QFM5	Schist	Qtz,Fsp, Bt,Chl		Good foliation, Bt altered to Chl
QMA1	Amphibolite	Am,Qtz,Fsp	Op,Chl,Bt	

Notes: Major minerals are in order of their abundance in thin sections and accessory minerals are arranged alphabetically. Mineral abbreviation are as follows: Am, Amphibole; Bt, Biotite; Cb, Carbonate mineral; Chl, Chlorite; Ep, Epidote; Fsp, Feldspar; Ky , Kyanite; Ms, Muscovite; Op, Opaque; Opx, Orthopyroxene; Pl, Plagioclase; Qtz, Quartz; Ser, Sericite; Ttn, Titanite; Tur, Tourmaline.

Table A2. Li concentrations and isotopic compositions of pure Li solutions of reference materials IRMM-016 and UMD-1.

Time Stamp	δ^7Li	[Li] (ppb)	
IRMM-016 (50ppb)			
2008 06 20 16:48	0.10	53.2	
2008 06 20 21:52	1.64	54.0	
2008 07 11 10:35	1.23	48.8	
2008 07 11 17:17	-0.20	49.6	
2008 07 11 23:02	0.64	49.1	
2008 07 17 16:00	0.13	48.0	
2008 07 17 23:38	-0.74	46.7	
2008 07 18 03:11	-1.05	45.6	
2008 09 16 16:27	-0.74	50.3	
2008 09 16 22:19	-0.93	49.5	
2008 09 26 13:54	-0.78	51.5	
2008 09 26 21:57	-0.96	48.4	
2008 10 01 11:15	-0.05	51.6	
2008 10 01 16:00	-0.42	51.0	
2008 10 01 19:09	-0.50	50.0	
2008 10 02 01:33	-0.95	49.7	
2008 11 26 17:03	-0.83	53.8	
2008 11 26 21:51	-0.54	50.5	
2009 06 06 12:35	0.46	48.9	
2009 06 06 14:45	-0.69	53.9	
2009 06 06 18:09	-0.17	49.0	
2009 06 06 19:57	-0.52	49.8	
2009 06 07 00:19	-0.08	52.4	
2009 06 07 03:26	-0.36	51.0	
2009 06 18 10:50	-0.94	54.1	
2009 06 18 12:51	-0.73	51.5	
2009 06 18 15:33	-0.32	48.0	
average	-0.47	50.3	n=25
2σ stdev	0.92	4.4	
UMD-1 (50ppb)			
2008 06 20 16:27	54.17	53.8	
2008 06 20 21:32	55.56	55.1	
2008 06 21 01:54	55.21	50.2	
2008 07 11 10:15	54.04	53.1	
2008 07 11 16:57	54.05	53.0	
2008 07 11 22:41	54.54	52.7	
2008 07 17 15:40	54.84	55.1	
2008 07 17 23:18	55.00	55.2	
2008 07 18 02:50	54.88	53.8	

2008 09 16 16:07	53.31	55.2	
2008 09 16 21:59	52.71	54.9	
2008 09 26 21:36	55.39	51.1	
2008 10 01 10:55	54.08	50.3	
2008 10 01 15:40	54.39	54.2	
2008 10 02 01:13	53.94	54.5	
2008 11 26 16:43	53.73	55.0	
2008 11 26 21:30	54.00	56.3	
2009 06 06 12:15	54.99	51.4	
2009 06 06 14:18	54.41	53.4	
2009 06 06 17:49	55.20	53.2	
2009 06 06 19:37	54.46	49.0	
2009 06 07 03:06	54.83	53.3	
2009 06 18 10:30	53.73	57.8	
2009 06 18 12:31	54.06	57.9	
2009 06 18 15:13	53.89	51.7	
average	54.35	53.6	n=22
2σ stdev	1.05	4.5	

Table A3. Li concentrations and isotopic compositions of USGS rock standards.

Standard Name	Lab #	Date Run	[Li] (ppm)	δ^7Li	Source
Basalt, Hawaii					
BHVO-1	XL0819	6/20/08	5.4	3.3	this study
BHVO-1	XL0819r	7/17/08	6.4	4.3	this study
BHVO-1	XL0879	9/26/08	4.5	3.7	this study
BHVO-1	XL0880	10/1/08	5.2	4.7	this study
Average			5.4	4.0	this study
BHVO-1			4.3~5.3	4.7~5.8	GEOREM database
Andesite, Oregon					
AGV-1	XL0820	6/20/08	10.7	5.0	this study
AGV-1	XL0820r	7/17/08	9.4	4.6	this study
AGV-1	XL0881	9/16/08	10.4	4.5	this study
AGV-1	XL0882	10/1/08	11.1	4.4	this study
AGV-1	XL0883	10/1/08	10.1	4.2	this study
AGV-1	XL0883r	11/26/08	12.5	5.1	this study
Average			10.7	4.6	this study
AGV-1			10~12	6.7	Magna (2004)
Granite, Rhode Island					
G-2	XL0811	3/19/08	35.2	1.1	this study
G-2	XL0811r	11/26/08	40.8	1	this study
G-2	XL0885	9/26/08	32.9	-0.6	this study
G-2	XL0884	6/18/09	32.0	-0.5	this study
Average			35.2	0.3	this study
G-2			31~45	-1.2~-0.3	Tomascak (2004)

Note: External analytical uncertainties of [Li] and δ^7Li from this study are better than ±10% (2σ) and ±1 (2σ), respectively. "r"s at the end of the Lab #s indicate re-run the same sample solutions.

Table A4. Li concentrations in the BCR-2g standard.

Standard Name	[Li] (ppm)	Source
BCR-2g	9.6	this study
BCR-2g	10.0	this study
BCR-2g	10.9	this study
BCR-2g	9.7	this study
BCR-2g	9.5±1.8(2σ）	GEOREM database

Table A5. Major element concentrations of amphiboles.

	LP2	LP6	LP8	LP21	LP26	LP30	QMA1	average
SiO_2	40.4	39.7	39.9	40.2	39.9	40.5	42.7	40.5
TiO_2	0.4	0.5	0.3	0.4	0.2	0.4	0.4	0.4
Al_2O_3	15.5	16.1	17.8	16.9	15.3	13.7	14.4	15.7
FeO	24.1	24.6	23.4	23.8	26.9	26.1	19.8	24.1
MnO	0.3	0.2	0.3	0.2	0.4	0.5	0.2	0.3
MgO	3.8	3.4	3.8	3.4	2.0	3.4	7.0	3.8
CaO	11.7	11.6	11.4	11.6	11.3	11.8	11.6	11.6
Na_2O	1.1	1.0	1.2	1.3	1.1	1.2	1.3	1.2
K_2O	0.9	1.1	0.7	1.0	0.9	1.5	0.3	0.9
Total	98.2	98.3	98.6	98.9	97.9	98.9	97.7	98.4
2σ stdev of CaO	0.2	0.4	0.9	0.4	0.5	0.3	0.4	
# of spots	9	4	5	7	5	3	17	

Notes: [1].Each sample reported is the average of 3 to 17 spots. Major element values are in wt. %. “2σ of CaO” is the 2σ standard deviation of multiple measurements of the same samples.

Table A6. Li concentrations and isotopic compositions of the ARA southern profile (not modeled).

Sample #	Rock Type	[Li] (ppm)	δ^7Li	Distance (m)
Animikie Red Ace(Southern)				
ARA3a	Schist	126	4.5	0.
ARA3b	Schist	160	4.0	0.75
ARA3c	Schist	145	3.7	1.7
ARA3d	Schist	98	4.7	2.8
ARA3e	Schist	99	3.4	4.3
ARA4a	Schist	158	4.7	4.4
ARA4b1	Pegmatite	478	6.1	4.4
ARA4b2	Schist	287	3.7	4.42
ARA4b4	Schist	235	4.0	4.46
ARA4c	Schist	170	3.5	4.90
ARA4d	Schist	151	4.1	6.90
ARA4e	Schist	153	3.0	7.95
ARA4f	Schist	151	3.1	12.10
ARA4g	Schist	152	3.4	17.80
ARA4h	Schist	114	1.9	21.40
ARA4i	Schist	195	1.3	23.40

Note: [1] $^{(\#)}$: Times of re-runs on ICP-MS from the same sample solution and values reported are therefore averages of re-runs.

References

Ague, J.J., 2003. Fluid flow in the deep crust. In: D.H. Heinrich and K.T. Karl (Editors), Treatise on Geochemistry. The crust. Pergamon, Oxford, pp. 195-228.

Baumgartner, L.P. and Valley, J.W., 2001. Stable isotope transport and contact metamorphic fluid flow, Stable Isotope Geochemistry. Reviews in Mineralogy & Geochemistry, pp. 415-467.

Bercovici, D., Ricard, Y. and Schubert, G., 2001. A two-phase model for compaction and damage 1. General Theory. Journal of Geophysical Research-Solid Earth, 106, 8887-8906.

Bickle, M.J. and McKenzie, D., 1987. The transport of heat and matter by fluids during metamorphism. Contributions to Mineralogy and Petrology, 95, 384-392.

Bowman, J.R. and Willett, S.D., 1991. Spatial patterns of oxygen isotope exchange during one-dimensional fluid infiltration. Geophysical Research Letters, 18, 971-974.

Connolly, J.A.D., 1997. Devolatilization-generated fluid pressure and deformation-propagated fluid flow during prograde regional metamorphism. Journal of Geophysical Research-Solid Earth, 102, 18149-18173.

Connolly, J.A.D. and Podladchikov, Y.Y., 1998. Compaction-driven fluid flow in viscoelastic rock. Geodinamica Acta, 11, 55-84.

Cook, S.J., Bowman, J.R. and Forster, C.B., 1997. Contact metamorphism surrounding the Alta stock: Finite element model simulation of heat- and O-18/O-16 mass-transport during prograde metamorphism. American Journal of Science, 297, 1-55.

Cui, X.J., Nabelek, P.I. and Liu, M., 2001. Heat and fluid flow in contact metamorphic aureoles with layered and transient permeability, with application to the Notch Peak aureole, Utah. Journal of Geophysical Research-Solid Earth, 106, 6477-6491.

Cui, X.J., Nabelek, P.I. and Liu, M.A., 2002. Numerical modeling of fluid flow and oxygen isotope exchange in the Notch Peak contact-metamorphic aureole, Utah. Geological Society of America Bulletin, 114, 869-882.

Deming, D., 1994. Fluid flow and heat transport in the upper continental crust. Geological Society London Special Publications, 78, 27.

Drew, D. and Passman, S., 1999. Theory of multicomponent flow, 135. Springer Verlag, NY.

Ferry, J.M., 1994. A historical review of metamorphic fluid-flow. Journal of Geophysical Research-Solid Earth, 99, 15487-15498.

Ferry, J.M., Wing, B.A., Penniston-Dorland, S.C. and Rumble, D., 2002. The direction of fluid flow during contact metamorphism of siliceous carbonate rocks: new data for the Monzoni and Predazzo aureoles, northern Italy, and a global review. Contributions to Mineralogy and Petrology, 142, 679-699.

Fritz, S.J., 1992. Measuring the ratio of aqueous diffusion-coefficients between (LI+CL-)-LI-6 and (LI+CL-)-LI-7 by osmometry. Geochimica Et Cosmochimica Acta, 56, 3781-3789.

Hier-Majumder, S., Ricard, Y. and Bercovici, D., 2006. Role of grain boundaries in magma migration and storage. Earth and Planetary Science Letters, 248, 735-749.

Holm, D.K., Van Schmus, W.R., MacNeill, L.C., Boerboom, T.J., Schweitzer, D. and Schneider, D., 2005. U-Pb zircon geochronology of Paleoproterozoic plutons from the northern midcontinent, USA: Evidence for subduction flip and continued convergence after geon 18 Penokean orogenesis. Geological Society of America Bulletin, 117, 259-275.

Huenges, E., Erzinger, J., Kuck, J., Engeser, B. and Kessels, W., 1997. The permeable crust: Geohydraulic properties down to 9101 m depth. Journal of Geophysical Research-Solid Earth, 102, 18255-18265.

Manning, C.E. and Ingebritsen, S.E., 1999. Permeability of the continental crust: Implications of geothermal data and metamorphic systems. Reviews of Geophysics, 37, 127-150.

Marks, M.A.W., Rudnick, R.L., McCammon, C., Vennemann, T. and Markl, G., 2007. Arrested kinetic Li isotope fractionation at the margin of the Ilimaussaq complex, South Greenland: Evidence for open-system processes during final cooling of peralkaline igneous rocks. Chemical Geology, 246, 207-230.

McKenzie, D., 1984. The generation and compaction of partially molten rock. Journal of Petrology, 25, 713-765.

Moriguti, T. and Nakamura, E., 1998. High-yield lithium separation and the precise isotopic analysis for natural rock and aqueous samples. Chemical Geology, 145, 91-104.

Norton, D. and Taylor, H.P., 1979. Quantitative simulation of the hydrothermal systems of crystallizing magmas on the basis of transport-theory and oxygen isotope data - analysis of the Skaergaard intrusion. Journal of Petrology, 20, 421-486.

Patankar, S.V., 1980. Numerical heat transfer and fluid flow. Taylor & Francis, 197 pp.

Ricard, Y., Bercovici, D. and Schubert, G., 2001. A two-phase model for compaction and damage 2. Applications to compaction, deformation, and the role of interfacial surface tension. Journal of Geophysical Research-Solid Earth, 106, 8907-8924.

Richter, F.M., Davis, A.M., DePaolo, D.J. and Watson, E.B., 2003. Isotope fractionation by chemical diffusion between molten basalt and rhyolite. Geochimica Et Cosmochimica Acta, 67, 3905-3923.

Richter, F.M., Liang, Y. and Davis, A.M., 1999. Isotope fractionation by diffusion in molten oxides. Geochimica Et Cosmochimica Acta, 63, 2853-2861.

Richter, F.M. and McKenzie, D., 1984. Dynamical Models for Melt Segregation from a Deformable Matrix. Journal of Geology, 92, 729-740.

Richter, F.M., Mendybaev, R.A., Christensen, J.N., Hutcheon, I.D., Williams, R.W., Sturchio, N.C. and Beloso, A.D., 2006. Kinetic isotopic fractionation during diffusion of ionic species in water. Geochimica Et Cosmochimica Acta, 70, 277-289.

Rudnick, R.L., Tomascak, P.B., Njo, H.B. and Gardner, L.R., 2004. Extreme lithium isotopic fractionation during continental weathering revealed in saprolites from South Carolina. Chemical Geology, 212, 45-57.

Scott, D.R. and Stevenson, D.J., 1984. Magma solutions. Geophysical Research Letters, 11, 1161-1164.

Sims, P., Schulz, K. and Peterman, Z., 1992. Geology and geochemistry of Early Proterozoic rocks in the Dunbar area, northeastern Wisconsin. US Geological Survey Professional Paper 1517, US Geological Survey, Reston, VA, pp. 65.

Sirbescu, M.L.C., Hartwick, E.E. and Student, J.J., 2008. Rapid crystallization of the Animikie Red Ace Pegmatite, Florence county, northeastern Wisconsin: inclusion microthermometry and conductive-cooling modeling. Contributions to Mineralogy and Petrology, 156, 289-305.

Teng, F.Z., McDonough, W.F., Rudnick, R.L., Dalpe, C., Tomascak, P.B., Chappell, B.W. and Gao, S., 2004. Lithium isotopic composition and concentration of the upper continental crust. Geochimica Et Cosmochimica Acta, 68, 4167-4178.

Teng, F.Z., McDonough, W.F., Rudnick, R.L. and Walker, R.J., 2006a. Diffusion-driven extreme lithium isotopic fractionation in country rocks of the Tin Mountain pegmatite. Earth and Planetary Science Letters, 243, 701-710.

Teng, F.Z., McDonough, W.F., Rudnick, R.L., Walker, R.J. and Sirbescu, M.L.C., 2006b. Lithium isotopic systematics of granites and pegmatites from the Black Hills, South Dakota. American Mineralogist, 91, 1488-1498.

Teng, F.Z., McDonough, W.F., Rudnick, R.L. and Wing, B.A., 2007. Limited lithium isotopic fractionation during progressive metamorphic dehydration in metapelites: A case study from the Onawa contact aureole, Maine. Chemical Geology, 239, 1-12.

Tomascak, P.B., 2004. Developments in the understanding and application of lithium isotopes in the earth and planetary sciences, Geochemistry of Non-Traditional Stable Isotopes. Reviews in Mineralogy & Geochemistry, pp. 153-195.

Walther, J.V. and Orville, P.M., 1982. Volatile production and transport in regional metamorphism. Contributions to Mineralogy and Petrology, 79, 252-257.

Wunder, B., Meixner, A., Romer, R.L., Feenstra, A., Schettler, G. and Heinrich, W., 2007. Lithium isotope fractionation between Li-bearing staurolite, Li-mica and aqueous fluids: An experimental study. Chemical Geology, 238, 277-290.

Wunder, B., Meixner, A., Romer, R.L. and Heinrich, W., 2006. Temperature-dependent isotopic fractionation of lithium between clinopyroxene and high-pressure hydrous fluids. Contributions to Mineralogy and Petrology, 151, 112-120.